

LEARNED INFINITE ELEMENTS*

THORSTEN HOHAGE[†], CHRISTOPH LEHRENFELD[‡], AND JANOSCH PREUSS[§]

Abstract. We study the numerical solution of scalar time-harmonic wave equations on unbounded domains which can be split into a bounded interior domain of primary interest and an exterior domain with separable geometry. To compute the solution in the interior domain, approximations to the Dirichlet-to-Neumann (DtN) map of the exterior domain have to be imposed as transparent boundary conditions on the artificial coupling boundary. Although the DtN map can be computed by separation of variables, it is a nonlocal operator with dense matrix representations, and hence computationally inefficient. Therefore, approximations of DtN maps by sparse matrices, usually involving additional degrees of freedom, have been studied intensively in the literature using a variety of approaches including different types of infinite elements, local non-reflecting boundary conditions, and perfectly matched layers. The entries of these sparse matrices are derived analytically, e.g. from transformations or asymptotic expansions of solutions to the differential equation in the exterior domain. In contrast, in this paper we propose to ‘learn’ the matrix entries from the DtN map in its separated form by solving an optimization problem as a preprocessing step. Theoretical considerations suggest that the approximation quality of learned infinite elements improves exponentially with increasing number of infinite element degrees of freedom, which is confirmed in numerical experiments. These numerical studies also show that learned infinite elements outperform state-of-the-art methods for the Helmholtz equation. At the same time, learned infinite elements are much more flexible than traditional methods as they, e.g., work similarly well for exterior domains involving strong reflections. As main motivating example we study the atmosphere of the Sun, which is strongly inhomogeneous and exhibits reflections at the corona.

Key words. transparent boundary conditions, Dirichlet-to-Neumann map, helioseismology, learning, infinite elements, rational approximation, Helmholtz equation

AMS subject classifications. 65N30, 35L05, 35J05, 33C10, 85-08

1. Introduction. To treat time-harmonic wave equations posed on unbounded domains with a numerical discretization, an artificial boundary is typically introduced to obtain a finite computational domain. On this artificial boundary appropriate boundary conditions need to be imposed to ensure that the discrete solution on the computational domain is a good approximation of the restriction of the true solution on the unbounded domain. Such conditions are called absorbing or transparent boundary conditions. A large variety of transparent boundary conditions is available in the literature, see [25, 17]. As one class of such methods, infinite elements have been devised and analyzed since the 1970s for a variety of problems. We only refer to [39, 8, 14, 3, 28]. As an alternative, (low order) *local* non-reflecting boundary conditions have been proposed since the end of the 1970s, see [15, 6] for two prominent examples. Later also high-order local non-reflecting boundary conditions using auxiliary variables were developed, see [18, 19, 20]. Finally we mention – as probably the most prominent candidate – Perfectly Matched Layers (PML) [7].

Despite the wide variety of approaches, research on transparent boundary conditions is far from finished since for many important problems established methods encounter severe difficulties. In particular, this work has been initiated by challenges in the simulation of acoustic waves in computational helioseismology [22, 23]. He-

*Submitted to the editors DATE.

[†]Institut für Numerische und Angewandte Mathematik, Universität Göttingen and Max-Planck-Institut für Sonnensystemforschung, Göttingen, (hohage@math.uni-goettingen.de).

[‡]Institut für Numerische und Angewandte Mathematik, Universität Göttingen, (lehrenfeld@math.uni-goettingen.de).

[§]Institut für Numerische und Angewandte Mathematik, Universität Göttingen and Max-Planck-Institut für Sonnensystemforschung, Göttingen, (j.preuss@math.uni-goettingen.de).

lioseismology studies the solar interior by analyzing oscillation data measured at the visible solar surface (photosphere). Sound speed and density are strongly varying (nonanalytic) functions in the solar atmosphere (see [Figure 2a](#)) rendering perfectly matched layers, classical infinite elements or approaches based on Green's functions inapplicable. State-of-the-art local transparent boundary conditions ([\[16, 4, 5\]](#)) based on strongly simplified models of the solar atmosphere and their limitations will be discussed in [subsection 3.4](#).

All approaches discussed above are derived from analytical studies of the differential equation in the exterior domain. In this paper we will access the exterior differential equation only implicitly via the associated DtN map on the coupling boundary. We propose to ‘learn’ infinite elements from this DtN map in a preprocessing step in situations where the DtN map can be computed by separation of variables. To outline the main ideas, let Γ denote the coupling boundary between the interior and the exterior domain, let Δ_Γ be the Laplace-Beltrami operator on Γ , and suppose that the exterior PDE is separable with respect to eigenpairs (λ_ℓ, v_ℓ) of $-\Delta_\Gamma$ where $\{v_\ell : \ell \in \mathbb{N}\}$ forms a complete orthonormal system of $L^2(\Gamma)$. Then the DtN map can be written as a functional calculus

$$\mathcal{DtN}u_0 = dtn(-\Delta_\Gamma)u_0 = \sum_{\ell=1}^{\infty} dtn(\lambda_\ell) \langle u_0, v_\ell \rangle v_\ell,$$

where the complex-valued function dtn is initially defined on the spectrum of $-\Delta_\Gamma$ by quotients of derivatives and function values of separated ordinary differential equations. This formula, which will be rederived in [section subsection 3.1](#), can be found in many places (see, e.g., [section 3.2](#) of [\[29\]](#)), although the interpretation as a functional calculus is less common. It turns out that dtn has a natural analytic extension to a neighborhood in the complex plane.

In a nutshell, learned infinite elements take the algebraic structure of classical infinite element discretizations as in [\[3, 14\]](#) and optimize over the infinite element matrix entries such that the Schur complement of these matrix entries provides the best possible approximation to the Dirichlet-to-Neumann map \mathcal{DtN} . Here and in the following by Schur complement we always mean the Schur complement restricted to the boundary degrees of freedom. Since we optimize the Schur complement of the infinite element matrix entries, the shape functions corresponding to these matrix entries become irrelevant. In contrast to classical infinite elements, our approach only provides an approximation of the interior solution, but no approximation of the exterior solution at all. (Note that shape functions of different types of infinite elements would provide different values of the exterior solution!) If the solution in the exterior domain is required as well, it can be evaluated in a postprocessing step using integral representations and fast summation techniques (see, e.g., [\[24\]](#)). For a given accuracy, this may be more efficient than a direct approximation by classical infinite elements since a smaller computational domain and less exterior degrees of freedom are needed.

In this paper we study the situation that the computational domain is surrounded by a layer of infinite elements in tensor product form. Note that a layer of tensor product finite elements leads to the same algebraic structure of the system matrix, and also the case of a finite number of tensor product finite element layers, which occurs in particular in tensor product PML discretizations, is a special case of this algebraic structure. We will show in [section 2](#) and [section 5](#) that the Schur complement of the exterior degrees of freedom in system matrices of this structure can be expressed in terms of the discrete version $-\Delta_{\Gamma,h}$ of the Laplace-Beltrami operator on Γ corre-

sponding to the finite element discretization of the boundary Γ . More precisely, if $(\underline{\lambda}_\ell, \underline{v}_\ell)$ are eigenpairs of $-\Delta_{\Gamma,h}$ which are orthonormal in the discrete approximation $\langle \cdot, \cdot \rangle_h$ of the L^2 inner product, we show that the Schur complement is described by a discrete DtN map of the form

$$\text{DtN } \underline{u}_0 = \text{dtn}(-\Delta_{\Gamma,h}) \underline{u}_0 = \sum_{\ell} \text{dtn}(\underline{\lambda}_\ell) \langle \underline{u}_0, \underline{v}_\ell \rangle_h \underline{v}_\ell$$

with a complex-valued rational function dtn .

Therefore, we end up with a rational approximation problem. More precisely, we have to find a function $\text{dtn}(\lambda) = p(\lambda)/q(\lambda)$ with complex polynomials p and q of degrees $N+1$ and N , respectively, that best approximates the function dtn with respect to some norm. Here N is the number of exterior degrees of freedom per degree of freedom on the boundary, and dtn is defined in terms of the $(N+1) \times (N+1)$ components of the local system matrices of the infinite elements, over which we optimize. After a reduction step the number of unknowns grows only linearly with N . Due to the meromorphic extension property of the function dtn we can appeal to results in rational approximation theory to show that the approximation error decreases exponentially in N , at least on bounded intervals.

While the approach can easily be generalized to most other discretization schemes, in this article we will consider the finite element method as the underlying discretization of the interior domain for ease of presentation.

The remainder of this paper is structured as follows. In [section 2](#) we introduce the concept of learned infinite elements starting from a discrete algebraic point of view. A crucial assumption used in that section and throughout the whole paper is that the discrete differential operator associated to the exterior domain problem can be written in tensor product form. This requires that the same can be done at the continuous level. A corresponding class of PDE problems is discussed in [section 3](#), and several examples are given. The [section 4](#) is devoted to the approximation problem between dtn and dtn . Theoretical considerations suggest that even when the number of parameters in the ansatz for dtn arising from learned infinite elements is reduced to $O(N)$ the approximation should converge exponentially with increasing number N of infinite element degrees of freedom. In [section 5](#) we turn our attention to (finite element based) discretizations with tensor product form of the exterior domain including the generic form of learned infinite elements proposed in this paper. A variety of numerical experiments presented in [section 6](#) corroborates this finding. Both homogeneous problems which allow for a comparison with established transparent boundary conditions and first results for helioseismology are presented. The paper ends with a conclusion and outlook towards further research.

2. Tensor product Learned Infinite Elements. In this section we derive the learned infinite element approach at an algebraic discrete level.

2.1. Problem description. Suppose we have a finite element discretization of a linear PDE with a vector \underline{u}_I of degrees of freedom (DOFs) in the interior of the domain $\Omega_{\text{int}} \subset \mathbb{R}^d$, $d \in \mathbb{N}$ and a vector \underline{u}_Γ of DOFs on some boundary $\Gamma \subset \partial\Omega_{\text{int}}$. As a partitioned linear system we obtain

$$\begin{bmatrix} L_{II} & L_{I\Gamma} \\ L_{\Gamma I} & L_{\Gamma\Gamma}^{\text{int}} \end{bmatrix} \begin{bmatrix} \underline{u}_I \\ \underline{u}_\Gamma \end{bmatrix} = \begin{bmatrix} \underline{f}_I \\ \underline{f}_\Gamma^{\text{int}} + \underline{f}_\Gamma^{\text{N}} \end{bmatrix}.$$

Here $L_{\Gamma\Gamma}^{\text{int}}$ and $\underline{f}_\Gamma^{\text{int}}$ represent couplings and sources stemming from the interior discretization, especially volume terms from Ω_{int} close to Γ . $\underline{f}_\Gamma^{\text{N}} = M \underline{v}^{\text{N}}$ where \underline{v}^{N}

represents the Neumann data (or more generally the right hand side of the natural boundary condition, but we will assume that both coincide) and M is the mass matrix of the finite element discretization on Γ , i.e. $M_{ij} = \int_{\Gamma} \phi_i \phi_j \, d\hat{x}$ and ϕ_i denote the shape functions on Γ such that \underline{u}_{Γ} represents the function $\sum_i (\underline{u}_{\Gamma})_i \phi_i$.

In this paper we only study the solution of PDEs on unbounded domains $\Omega \subset \mathbb{R}^d$ so that the Neumann data \underline{v}^N is not given but is rather the result of the solution of a linear, homogeneous *exterior* problem on $\Omega_{\text{ext}} = \Omega \setminus \overline{\Omega_{\text{int}}}$ for the Dirichlet data provided by \underline{u}_{Γ} . The one-to-one relation between \underline{u}_{Γ} and \underline{v}^N is encoded in the Dirichlet-to-Neumann operator DtN^{ext} ($\underline{v}^N = -\text{DtN}^{\text{ext}} \underline{u}_{\Gamma}$), a tool that plays an important role also in other domain decomposition methods in the quest for appropriate transmission conditions [38]. The DtN^{ext} operator is a dense matrix and allows to write the problem as

$$\begin{bmatrix} L_{II} & L_{I\Gamma} \\ L_{\Gamma I} & L_{\Gamma\Gamma}^{\text{int}} + M \text{DtN}^{\text{ext}} \end{bmatrix} \begin{bmatrix} \underline{u}_I \\ \underline{u}_{\Gamma} \end{bmatrix} = \begin{bmatrix} \underline{f}_I \\ \underline{f}_{\Gamma}^{\text{int}} \end{bmatrix}.$$

Since the use of the full matrix DtN^{ext} may be computationally inefficient, we wish to approximate this system of equations by a sparse system involving additional degrees of freedom \underline{u}_E :

$$\begin{bmatrix} L_{II} & L_{I\Gamma} & 0 \\ L_{\Gamma I} & L_{\Gamma\Gamma}^{\text{int}} + L_{\Gamma\Gamma} & L_{\Gamma E} \\ 0 & L_{E\Gamma} & L_{EE} \end{bmatrix} \begin{bmatrix} \underline{u}_I \\ \underline{u}_{\Gamma} \\ \underline{u}_E \end{bmatrix} = \begin{bmatrix} \underline{f}_I \\ \underline{f}_{\Gamma} \\ 0 \end{bmatrix}.$$

In other words, we wish to find sparse matrices $L_{\Gamma\Gamma}$, $L_{\Gamma E}$, $L_{E\Gamma}$ and L_{EE} of small size such that the Schur complement of L_{EE} approximates $M \text{DtN}^{\text{ext}}$:

$$(2.1) \quad \text{DtN}^{\text{ext}} \stackrel{!}{\approx} \text{DtN} \quad \text{with} \quad \text{DtN} := M^{-1} (L_{\Gamma\Gamma} - L_{\Gamma E} L_{EE}^{-1} L_{E\Gamma}).$$

2.2. Tensor product ansatz. In analogy to the mass matrix on Γ , let us introduce the stiffness matrix $K = (\int_{\Gamma} \nabla_{\Gamma} \phi_i \nabla_{\Gamma} \phi_j \, d\hat{x})_{ij}$ on the boundary Γ so that the discrete Laplace-Beltrami operator on Γ is $-\Delta_{\Gamma,h} = M^{-1}K$. Moreover, recall that the Kronecker (or tensor) product of an $m \times n$ matrix A and a $p \times q$ matrix B is the $mp \times nq$ block matrix given by

$$A \otimes B = \begin{bmatrix} a_{11}B & \dots & a_{1n}B \\ \vdots & \ddots & \vdots \\ a_{m1}B & \dots & a_{mn}B \end{bmatrix}.$$

In this paper we will study the tensor product ansatz

$$(2.2) \quad \begin{bmatrix} L_{\Gamma\Gamma} & L_{\Gamma E} \\ L_{E\Gamma} & L_{EE} \end{bmatrix} = A \otimes M + B \otimes K = \begin{bmatrix} A_{\Gamma\Gamma} & A_{\Gamma E} \\ A_{E\Gamma} & A_{EE} \end{bmatrix} \otimes M + \begin{bmatrix} B_{\Gamma\Gamma} & B_{\Gamma E} \\ B_{E\Gamma} & B_{EE} \end{bmatrix} \otimes K$$

with matrices $A, B \in \mathbb{C}^{(N+1) \times (N+1)}$ and $A_{\Gamma\Gamma}, B_{\Gamma\Gamma} \in \mathbb{C}$. Here N should be small, say of the order of 10. This ansatz is motivated by the fact that many successful transparent boundary conditions have this algebraic structure as detailed in [section 5](#).

In the following we will study for which class of matrices DtN^{ext} this ansatz can be successful. It has the advantage that only the small matrices A and B have to be ‘learned’. Of course, we could use more general matrices $L_{\Gamma\Gamma}$, $L_{\Gamma E}$, $L_{E\Gamma}$ and L_{EE} with more free parameters. This would enable the approximation of more general matrices DtN^{ext} , but for the examples we have in mind the ansatz (2.2) turns out to be successful.

2.3. Feasibility analysis. The following result analyzes the eigenvectors and eigenvalues of DtN.

PROPOSITION 2.1. *If $(\underline{\lambda}_\ell, \underline{v}_\ell)$ is an eigenpair of the discrete Laplace-Beltrami operator $-\Delta_{\Gamma,h} = M^{-1}K$ on Γ , then*

$$\text{DtN } \underline{v}_\ell = \text{dtn}(\underline{\lambda}_\ell) \underline{v}_\ell$$

with the rational function dtn defined, for $\lambda \in \mathbb{C}$ by

$$(2.3) \quad \text{dtn}(\lambda) := A_{\Gamma\Gamma} + \lambda B_{\Gamma\Gamma} - (A_{\Gamma E} + \lambda B_{\Gamma E})(A_{EE} + \lambda B_{EE})^{-1}(A_{E\Gamma} + \lambda B_{E\Gamma}).$$

Proof. For the first term in the definition of DtN, cf. (2.1), we have

$$\begin{aligned} M^{-1}L_{\Gamma\Gamma}\underline{v}_\ell &= M^{-1}(A_{\Gamma\Gamma} \otimes M + B_{\Gamma\Gamma} \otimes K)\underline{v}_\ell = M^{-1}(A_{\Gamma\Gamma}M\underline{v}_\ell + B_{\Gamma\Gamma}K\underline{v}_\ell) \\ &= M^{-1}(A_{\Gamma\Gamma}M\underline{v}_\ell + B_{\Gamma\Gamma}\lambda_\ell M\underline{v}_\ell) = (A_{\Gamma\Gamma} + \lambda_\ell B_{\Gamma\Gamma})\underline{v}_\ell. \end{aligned}$$

Using a similar computation and the rule $(C \otimes D)(E \otimes F) = (CE \otimes DF)$, we obtain

$$\begin{aligned} M^{-1}L_{\Gamma E}L_{EE}^{-1}L_{E\Gamma}\underline{v}_\ell &= M^{-1}[(A_{\Gamma E} + \lambda_\ell B_{\Gamma E}) \otimes M][(A_{EE} + \lambda_\ell B_{EE}) \otimes M]^{-1}[(A_{E\Gamma} + \lambda_\ell B_{E\Gamma}) \otimes M]\underline{v}_\ell \\ &= (A_{\Gamma E} + \lambda_\ell B_{\Gamma E})(A_{EE} + \lambda_\ell B_{EE})^{-1}(A_{E\Gamma} + \lambda_\ell B_{E\Gamma})(M^{-1}MM^{-1}M)\underline{v}_\ell \end{aligned}$$

for the second term. Putting both together yields the result. \square

If we orthonormalize the eigenvectors $\underline{v}_\ell \in \mathbb{R}^{n_\Gamma}$ with respect to the natural inner product $\langle \underline{v}, \underline{w} \rangle_M := \underline{v}^* M \underline{w}$ on \mathbb{C}^{n_Γ} , then applying DtN to the identity $\underline{v} = \sum_\ell \underline{v}_\ell \underline{v}_\ell^* M \underline{v}$ yields

$$\text{DtN} = \sum_\ell \text{dtn}(\lambda_\ell) \underline{v}_\ell \underline{v}_\ell^* M =: \text{dtn}(-\Delta_{\Gamma,h}).$$

In other words, DtN is a functional calculus at the discrete Laplace-Beltrami operator $-\Delta_{\Gamma,h}$ in the space \mathbb{C}^{n_Γ} equipped with the inner product $\langle \cdot, \cdot \rangle_M$. Therefore, we may hope to be able to approximate DtN^{ext} well using our ansatz (2.2) if it has the same property, i.e. if

$$(2.4) \quad \text{DtN}^{\text{ext}} = \text{dtn}^{\text{ext}}(-\Delta_{\Gamma,h})$$

for some function dtn^{ext} . Note that dtn is a rational function with numerator of degree $N - 1$ and nominator of degree N . With such rational function we may hope to interpolate dtn^{ext} at at most $O(N)$ points. However, our approach will only be efficient, if N can be chosen much smaller than n_Γ . Therefore, in order to at least approximate dtn^{ext} accurately on the spectrum of $-\Delta_{\Gamma,h}$ by a rational function of small degree, dtn^{ext} must have an extension to a well-behaved smooth function. Of course, every function defined on a finite subset of \mathbb{R} can be extended to an analytic function on \mathbb{R} or even \mathbb{C} in many ways, e.g. by polynomial interpolation. However, fast approximation rates only hold true if derivatives of such an extension satisfy reasonable bounds, and this is what we mean by 'well-behaved'. By Cauchy's integral formula, this holds true in particular if dtn^{ext} has an analytic extension to a complex neighborhood of the spectrum which does not grow too rapidly with the distance to the spectrum. There is one exception to this smoothness requirement which will turn out relevant: Of course, with our approach we can deal with isolated singularities described by poles of rational functions.

To summarize our results the ansatz (2.2) will be successful if

- the matrix DtN^{ext} diagonalizes in the basis of the eigenvectors of the discrete Laplace-Beltrami operator $-\Delta_{\Gamma,h}$ such that (2.4) holds and
- dtn^{ext} , initially defined on the spectrum of $-\Delta_{\Gamma,h}$ can be extended to a well-behaved smooth function, possibly with the exception of isolated poles.

3. DtN maps for separable PDEs and examples. In this section we turn to a continuous setting and show that the two criteria at the end of the previous section are typically satisfied for PDEs which are separable in the exterior domain.

3.1. Framework. Let us consider a domain $\Omega \subset \mathbb{R}^d$ consisting of a bounded interior domain Ω_{int} and an exterior domain Ω_{ext} , which is typically unbounded. More precisely, we assume that $\overline{\Omega} = \overline{\Omega}_{\text{int}} \cup \overline{\Omega}_{\text{ext}}$, $\Omega_{\text{int}} \cap \Omega_{\text{ext}} = \emptyset$, and the coupling boundary $\Gamma := \overline{\Omega}_{\text{int}} \cap \overline{\Omega}_{\text{ext}}$ is smooth. We consider a linear second-order elliptic PDE (elliptic in the sense that the principal part is elliptic)

$$(3.1) \quad \mathcal{L}u = f \quad \text{in } \Omega \quad + \quad \text{radiation condition},$$

such that $\text{supp } f \subset \overline{\Omega}_{\text{int}}$. The radiation conditions at infinity will be specified in the examples. If the boundary of Ω is not empty ($\partial\Omega \neq \emptyset$), then a boundary condition on $\partial\Omega$ is required in addition. Our main focus will be on the exterior Dirichlet problem

$$(3.2) \quad \begin{aligned} \mathcal{L}u &= 0 & \text{in } \Omega_{\text{ext}} & \quad + \quad \text{radiation condition,} \\ u &= u_0 & \text{on } \Gamma, \end{aligned}$$

for some Dirichlet data u_0 . The Dirichlet-to-Neumann map is defined by $\mathcal{DtN}(u_0) := \frac{\partial u}{\partial \nu}|_{\Gamma}$ where ν denotes the unit normal vector pointing into the exterior of Ω_{ext} .

We assume that there exists a diffeomorphism

$$(3.3a) \quad \begin{aligned} \Psi : [a, \infty) \times \Gamma &\rightarrow \overline{\Omega}_{\text{ext}} \text{ such that} \\ \Psi(\{a\} \times \Gamma) &= \Gamma, \end{aligned}$$

$$(3.3b) \quad |\partial_r \Psi(a, \hat{x})|_2 = 1, \quad \hat{x} \in \Gamma,$$

with the derivative ∂_r with respect to the first variable. Further, we assume that \mathcal{L} separates in the coordinates given by Ψ as follows:

$$(3.4) \quad (\mathcal{L}u) \circ \Psi = [\mathcal{A} \otimes \text{Id}_{\Gamma} + \mathcal{B} \otimes (-\Delta_{\Gamma})](u \circ \Psi)$$

Here \mathcal{A} is a second-order differential operator in r , \mathcal{B} is a multiplication operator on $L^2([a, \infty))$, Δ_{Γ} is the Laplace-Beltrami operator on Γ , and Id_{Γ} the identity operator on $L^2(\Gamma)$. Further recall that tensor products of linear operators are uniquely defined by $(A \otimes B)(v \otimes w) = Av \otimes Bw$, and for L^2 -functions v and w one has $(v \otimes w)(x, y) = v(x)w(y)$. (In other words, A acts on the first variable and B on the second variable.)

As before, let $\{\underline{v}_{\ell} : \ell \in \mathbb{N}\}$ be an orthonormal basis of $L^2(\Gamma)$ consisting of eigenvectors of $-\Delta_{\Gamma}$ with corresponding eigenvalues λ_{ℓ} . Such an orthonormal basis exists since the Laplace-Beltrami operator on a smooth compact manifold is self-adjoint and has a compact resolvent. To solve (3.1) in Ω_{ext} in the coordinates (r, \hat{x}) by separation of variables, we have to study the separated equations

$$(3.5a) \quad [\mathcal{A} + \lambda_{\ell}\mathcal{B}]\Lambda_r(\lambda_{\ell}) = 0 \quad \text{for } r \in [a, \infty),$$

$$(3.5b) \quad \Lambda_a(\lambda_{\ell}) = 1, \quad \Lambda_r \text{ satisfies the radiation condition.}$$

Then the radiating solution to $\mathcal{L}u = 0$ in Ω_{ext} with Dirichlet data $u|_{\Gamma} = u_0$ can be represented as

$$(3.6) \quad (u \circ \Psi)(r, \cdot) = \Lambda_r(-\Delta_{\Gamma})u_0 = \sum_{\ell=1}^{\infty} \Lambda_r(\lambda_{\ell}) \underline{v}_{\ell}(u_0, \underline{v}_{\ell})_{\Gamma}.$$

Since Neumann data (with the interior normal vector on Ω_{int}) are given by $-\partial_r(u \circ \Psi)|_{r=a}$, the Dirichlet-to-Neumann map $\mathcal{DtN} : u_0 \rightarrow -\partial_r(u \circ \Psi)|_{r=a}$ is given by

$$(3.7) \quad \mathcal{DtN} = dtn(-\Delta_{\Gamma}) \quad \text{with} \quad dtn(\lambda) := -\partial_r \Lambda_r(\lambda)|_{r=a}.$$

Often, analytical expressions for the solutions of (3.5a)-(3.5b) and consequently for dtn are known as the following examples show. Otherwise, these solutions can be obtained numerically at negligible costs by solving ordinary differential equations. This is how we proceed for the case of the solar atmosphere as considered in [Example 3.4](#).

3.2. Examples of (piecewise) homogeneous exterior domains. We first discuss two examples of homogeneous exterior domains. We will show in particular that the second criterion at the end of [section 2](#) is satisfied in the continuous setting since dtn -functions have natural analytic extensions to complex neighborhoods of the spectrum.

Example 3.1 (homogeneous Helmholtz equation in the exterior of a ball). We consider the exterior Dirichlet problem

$$(3.8a) \quad -\Delta u - k^2 u = 0 \quad \text{in } \Omega_{\text{ext}} := \{x \in \mathbb{R}^d : |x|_2 > a\},$$

$$(3.8b) \quad u = u_0 \quad \text{on } \Gamma = a\mathbb{S}^{d-1},$$

$$(3.8c) \quad \lim_{r \rightarrow \infty} r^{(d-1)/2} \left(\frac{\partial u}{\partial r} - iku \right) = 0 \quad r = |x|_2$$

which occurs in the modelling of waves scattered by bounded obstacles, either penetrable or impenetrable (see, e.g., [\[12\]](#) for more information). Setting

$$(3.9) \quad \Psi(r, \hat{x}) := \frac{r}{a} \hat{x} \quad \text{for } r \in [a, \infty), \hat{x} \in a\mathbb{S}^{d-1},$$

we obtain

$$(3.10) \quad (-\Delta u - k^2 u)(\Psi(r, \hat{x})) = \left(-r^{1-d} \partial_r(r^{d-1} \partial_r) - \frac{a^2}{r^2} \Delta_{\Gamma} - k^2 \text{Id} \right) (u \circ \Psi)(r, \hat{x}),$$

i.e. $\mathcal{A} = -r^{1-d} \partial_r(r^{d-1} \partial_r) - k^2 \text{Id}$ and $(\mathcal{B}v)(r) = \frac{a^2}{r^2} v(r)$. Therefore, (3.5a) is the Bessel differential equation. For $d = 2$ the solution satisfying (3.5b) is given by $\Lambda_r(\lambda) = H_{a\sqrt{\lambda}}^{(1)}(kr) / H_{a\sqrt{\lambda}}^{(1)}(ka)$ in terms of the Hankel function $H_{a\sqrt{\lambda}}^{(1)}$ of the first kind of order $a\sqrt{\lambda}$. This leads to the dtn -function

$$(3.11) \quad dtn^{\text{hom}}(\lambda) = \frac{-k}{H_{a\sqrt{\lambda}}^{(1)}(ka)} (H_{a\sqrt{\lambda}}^{(1)})'(ka).$$

This function is initially defined on the spectrum $\sigma(-\Delta_{\Gamma}) = \{(\ell/a)^2 : \ell \in \mathbb{N} \cup \{0\}\}$ where the order of the Hankel functions is integer-valued. However, Hankel functions can be defined also for complex-valued orders ν , and $H_{\nu}^{(1)}(x)$ is an entire function of

ν (see [34]). Due to the recurrence relation $2(H_\nu^{(1)})'(x) = H_{\nu-1}^{(1)}(x) - H_{\nu+1}^{(1)}(x)$, the derivative $(H_\nu^{(1)})'(x)$ with respect to x is an entire function of ν as well. Therefore, choosing the negative real axis $\mathbb{R}_- := \{-x : x \geq 0\}$ as branch cut of the square root function, dtn^{hom} is a meromorphic function on $\mathbb{C} \setminus \mathbb{R}_-$. [34] also contains analytical results, e.g. on the asymptotic behavior of the zeros of $H_\bullet^{(1)}(x)$ and hence of the poles of dtn^{hom} . These poles are plotted in Figure 1a using numerical computations.

For computing roots and poles of meromorphic functions we utilize a mesh-based technique presented in [32, 33]. First, roots and poles are isolated using adaptive mesh refinement driven by an analysis of the function's phase and then verified by applying a discretized version of the argument principle. The special functions for evaluating dtn at complex numbers are taken from the library `mpmath` [30].

Our next example concerns an inhomogeneous exterior domain involving a jump:

Example 3.2 (Exterior domain with a jump). We again consider the problem (3.8) in dimension $d = 2$, but now assume that k depends in a piecewise constant manner on r . More precisely, we assume that for some $a \leq R_J < \infty$ and $k_I, k_\infty > 0$ we have

$$(3.12) \quad k(r) = \begin{cases} k_I & r < R_J, \\ k_\infty & r > R_J. \end{cases}$$

From the boundary condition at $r = a$ and matching conditions at $r = R_J$ it follows that the dtn function is given by

$$dtn^{\text{jump}}(\lambda) = \zeta(a\sqrt{\lambda}), \quad \zeta(\nu) = -k_I [A_\nu J'_\nu(k_I a) + B_\nu Y'_\nu(k_I a)].$$

Here Y_ν denotes the Bessel function of the second kind of order ν . The constants A_ν and B_ν , which are derived in the appendix, depend on the problem parameters a, R_J, k_I and k_∞ .

The function $dtn^{\text{jump}}(\lambda)$ for $a = 1$, $R_J = 2$ and $k_I = 16$, and $k_\infty = 8$ is shown in Figure 1b. Additionally, the poles of its meromorphic extension are displayed which are all simple and located extremely close to the positive real axis. As a result, the behavior $dtn^{\text{jump}}(\lambda)$ on the domain of interest is essentially dominated by these poles. It is then natural to expect and will later be confirmed in numerical experiments that an excellent fit of dtn^{jump} may be obtained by means of a rational approximation with a few simple poles.

Example 3.3 (Helmholtz equation in a wave-guide). Let $\tilde{\Gamma} \subset \mathbb{R}^{d-1}$ be a smooth, bounded domain and define $\Gamma := \{a\} \times \tilde{\Gamma}$ for some $a \in \mathbb{R}$ and

$$\Psi(r, \hat{x}) := \begin{pmatrix} r - a \\ 0 \end{pmatrix} + \tilde{x} \quad \text{for } r \in [a, \infty), \hat{x} \in \Gamma.$$

We consider the Helmholtz equation

$$(3.13) \quad \begin{aligned} (-\Delta - k^2)u &= 0 & \text{in } \Omega_{\text{ext}} &:= (a, \infty) \times \tilde{\Gamma} \\ u &= 0 & \text{on } (a, \infty) \times \partial\tilde{\Gamma} \end{aligned}$$

together with a radiation condition that will be discussed below. Let Δ_Γ denote the Laplace-Beltrami operator on Γ with Dirichlet boundary conditions. Then obviously

$$(-\Delta u - k^2 u)(\Psi(r, \hat{x})) = (-\partial_r^2 - \Delta_\Gamma - k^2)(u \circ \Psi)(r, \hat{x}),$$

i.e. $\mathcal{A} = -\partial_r^2 - k^2 \text{Id}$ and $\mathcal{B} = \text{Id}$. Therefore, (3.5a) has the two independent solutions $\exp(\pm i\sqrt{k^2 - \lambda_\ell}(\cdot - a))$. Here we choose the negative imaginary axis as branch cut of the square root function. Moreover, we assume that

$$(3.14) \quad k^2 \notin \sigma(-\Delta_\Gamma).$$

Then we say that a solution to (3.13) satisfies the radiation condition if it has an expansion (3.6) in terms of the functions $\Lambda_r(\lambda_\ell) := \exp(i\sqrt{k^2 - \lambda_\ell}(r - a))$.

This leads to the dtn function

$$dtn^{\text{guide}}(\lambda) = -i\sqrt{k^2 - \lambda}.$$

Under the assumption (3.14) it has a holomorphic extension to a neighborhood of $\sigma(-\Delta_\Gamma)$ (see Figure 1c). However, due to the branch cut singularity it does not have a natural meromorphic extension to the entire complex plane.

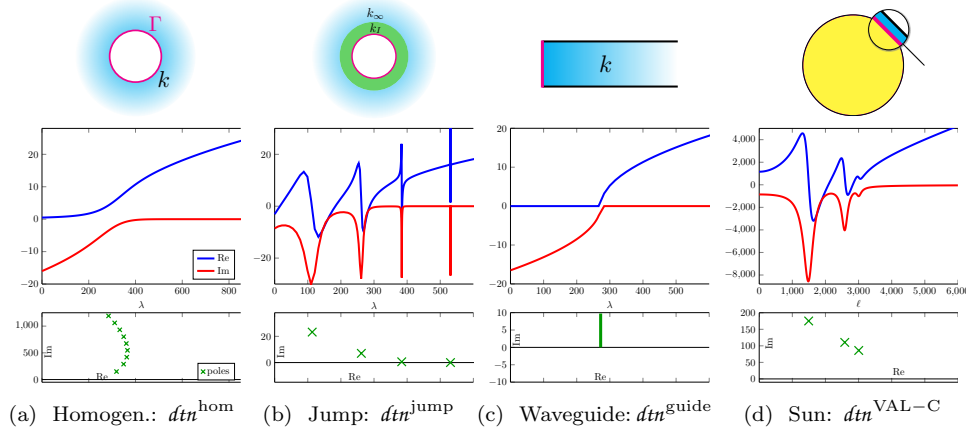


FIG. 1. Comparison of the dtn functions considered in this paper: (a): homogeneous Helmholtz equation in the exterior of a ball (Example 3.1), (b) same as (a) with jumping coefficient (Example 3.2), (c) homogeneous wave-guide with Dirichlet boundary conditions (Example 3.3), (d) VAL-C model of the solar atmosphere with Neumann condition at the corona (Example 3.4). First row: geometries, second row: real and imaginary part of the dtn functions, third row: structure of the singularities of analytic extensions of the dtn functions, which are poles in (a), (b) and (d), and a branch cut in (c).

3.3. A structural argument for the analyticity of dtn . In the examples of the previous subsection, analytic extensions could be derived from the explicit form of the dtn -function. In the following, we wish to provide a more structural argument for the existence of such natural extensions which is also applicable if dtn cannot be computed explicitly:

A main difficulty in the analysis of the boundary value problems (3.5) defining dtn is the treatment of the radiation condition, which is a condition on the asymptotic behavior at infinity. As we are only interested in the dtn -function, we may use a transformation of the differential equation, which allows to incorporate the radiation condition in the function space and leads to the same dtn function. The most prominent methods are Perfectly Matched Layers (PMLs) which formulate a differential equation for the analytic extensions $\tilde{\Lambda}_r(\lambda)$ of $r \mapsto \Lambda_r(\lambda)$ to a certain path in the

complex plane (see [subsection 5.2](#) for more details). This is done such that the radiation condition is satisfied if and only if the analytic extension is bounded. Therefore, $\tilde{\Lambda}_r(\lambda)$ is characterized by a boundary value problem $[\tilde{\mathcal{A}} + \lambda\tilde{\mathcal{B}}]\tilde{\Lambda}_r(\lambda) = 0$, $\tilde{\Lambda}_a(\lambda) = 1$, which is of the same form as (3.5), but without the radiation condition. If $\tilde{\mathcal{A}} + \lambda\tilde{\mathcal{B}}$ is a Fredholm operator for all λ in some domain $D \subset \mathbb{C}$ and $\tilde{\mathcal{A}} + \lambda\tilde{\mathcal{B}}$ is invertible for at least one $\lambda \in D$ (e.g. $\lambda \in \sigma(-\Delta_\Gamma)$), then by analytic Fredholm theory $\lambda \mapsto \tilde{\Lambda}_r(\lambda)$ is a function-valued meromorphic mapping on D , and hence dtn is a meromorphic function on D .

This situation occurs in Examples 3.1 and 3.2. In [Example 3.3](#) the branch cut occurs since the PML formulation breaks down for $\lambda = k^2$.

3.4. Models of the solar atmosphere. We now discuss in more detail PDE models in helioseismology as mentioned already in the introduction. Although more complex systems of differential equations have been derived to describe solar (and more generally stellar) oscillations, it has been shown in [21] that the scalar time-harmonic wave equation

$$(3.15) \quad -\operatorname{div} \left(\frac{1}{\rho} \nabla u \right) - \frac{\sigma^2}{\rho c^2} u = 0$$

captures the physics of oscillating pressure modes in the Sun to a reasonable extent. $\sigma = \omega + i\gamma$ contains the frequency $\omega > 0$ and a positive absorption coefficient $\gamma(r) > 0$. In the solar atmosphere, sound speed c and density ρ essentially depend only on the radial variable r , but they are usually nonanalytic functions derived from tabulated values that vary over several orders of magnitude (see [Figure 2a](#)). We use the VAL-C model proposed in [40] here combined with Models S [10] for the solar interior. Whereas pressure decreases sharply and monotonically, sound speed first decreases in the solar atmosphere and then increases again towards the corona, which is related to an increase of temperature from about 5000°C at the photosphere to several million °C in the corona. In the so-called convection zone, which comprises that upper 28% of the solar interior, first order terms in (3.15) play a dominant role. Since our focus is on the solar atmosphere, we have omitted this term in (3.15). Note that in this form, (3.15) satisfies the separation condition (3.4) with Ψ given by (3.9), $\mathcal{A} = -r^{1-d}\partial_r(r^{d-1}\frac{1}{\rho}\partial_r) - \frac{\sigma^2}{\rho c^2}\operatorname{Id}$ and $(\mathcal{B}v)(r) = \frac{a^2}{r^2}v(r)$.

Example 3.4 (transformed equation for solar sound waves). Instead of directly working with equation (3.15) we follow the literature, see e.g. [1, 5] and perform a transformation to a Schrödinger-type equation with an effective potential v by means of the substitution $u = \sqrt{\rho}\tilde{u}$. This yields the equation

$$(3.16a) \quad (-\Delta + v)\tilde{u} = 0 \quad \text{with} \quad v = \rho^{1/2}\Delta(\rho^{-1/2}) - \sigma^2/c^2.$$

Of course, (3.16a) also satisfies the separation condition (3.4) with Ψ given by (3.9), $\mathcal{A} = -r^{1-d}\partial_r(r^{d-1}\partial_r) + v$ and $(\mathcal{B}w)(r) = \frac{a^2}{r^2}w(r)$. Since the absorption coefficient $\gamma = \Im\sigma$ is positive, it suffices to impose boundedness as radiation condition. Alternatively, we may just impose a homogeneous Neumann condition close to the corona at a distance R_V from the center where the influence of pressure on the movement of matter becomes negligible and the PDE models (3.15) and (3.16a) break down:

$$(3.16b) \quad \tilde{u} = u_0 \quad \text{on } a\mathbb{S}^2$$

$$(3.16c) \quad \partial_r \tilde{u} = 0 \quad \text{on } R_V\mathbb{S}^2.$$

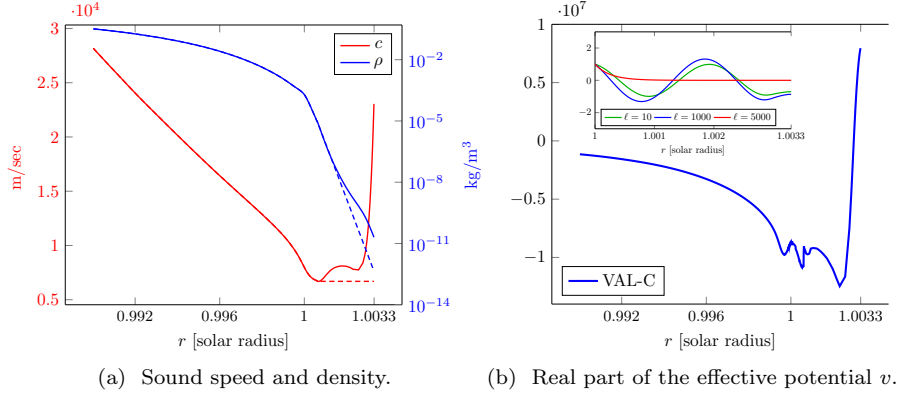


FIG. 2. Background coefficients for the Sun. Dashed lines in the left plot indicate a simplified model used in [4, 16]. The right plot shows the corresponding effective potential after transformation to a Schrödinger-type equation at 7.0 mHz. Additionally, some of the functions $\Re(\Lambda_r(\lambda_\ell))$ appearing in the computation of $dtn^{\text{VAL-C}}$ are displayed in the small inset.

A small frequency dependent damping is added as described in Section 7.3 of [21]. The coupling boundary Γ is positioned directly at the solar surface, i.e. $a = 1.0$ (in terms of the solar radius).

For realistic sound speed and density as given by the VAL-C model, the dtn function admits no analytical expression. Hence, the values $dtn^{\text{VAL-C}}(\lambda)$ have to be computed by solving the ODE (3.5a) with Dirichlet condition at $r = a$ and Neumann condition at $r = R_V$. However, one can apply the argument of subsection 3.3 to show the existence of a natural meromorphic extension of $dtn^{\text{VAL-C}}$. In fact, by standard arguments using compactness of embeddings one can see that the weak formulation of (3.16) leads to a Fredholm operator of index 0. Moreover, since $\gamma > 0$ it can be shown to be injective by taking the imaginary part of the variational formulation. Therefore, the operator is also surjective, and (3.16) is well-posed.

The values of $dtn^{\text{VAL-C}}$ at the eigenvalues λ_ℓ for a frequency of 7.0 mHz are shown in Figure 2. These values were obtained by solving an ODE for which we discretized the interval $[a, R_V]$ with one hundred equidistant finite elements of order eight. The potential well produced by the increase in sound speed apparently leads to a similar behavior as the discontinuous wavespeed considered in subsection 6.3. However, due to the huge magnitude of the potential extremely large modes (note the scaling of the abscissa) are required to capture the behavior of $dtn^{\text{VAL-C}}$.

As current state-of-the-art in computational local helioseismology, local non-reflecting boundary conditions for a simplified model of the solar atmosphere (so-called *atmospheric radiation conditions*) have been proposed and validated in [4, 16]. In this simplified model it is assumed that density decays exponentially and the sound speed is constant (see Figure 2a). This simplification (even without further approximations) only yields reasonable results if the coupling boundary is placed a few hundred kilometers above the photosphere whereas our approach offers the possibility to place the coupling boundary on the photosphere. This allows for a significant reduction of the number of DOFs. Moreover, the spikes in $dtn^{\text{VAL-C}}$ displayed in Figure 1d are not captured in this simplified model. They seem to be associated with reflections at the solar corona, which are discussed in [16] as potential reason for certain discrepancies

between their simulation results and helioseismic observations.

4. Approximation of dtn functions. The idea of learned infinite elements is to optimize the parameters A and B in the discrete DtN function dtn , cf. [section 2](#), representing the approximate transparent boundary conditions to achieve an optimal fit of the true DtN function dtn . A corresponding minimization problem is formulated in [subsection 4.1](#). A more efficient reduced ansatz for the matrices A and B is introduced in [subsection 4.2](#) and its use is demonstrated in [subsection 4.3](#). This reduction exposes dtn as a rational approximation of dtn with simple poles. Convergence of this approximation is discussed in [subsection 4.4](#).

4.1. The minimization problem. We are now in a position to define misfit function and minimization problem for the task of finding optimal A, B .

DEFINITION 4.1. *Let λ_ℓ be the continuous eigenvalues of the Laplace-Beltrami operator on Γ . Denote by $\mathit{dtn}(\lambda_\ell)$ the DtN numbers obtained from solving the ordinary differential equations [\(3.5a\)](#). Further, let $\mathit{dtn}(\lambda_\ell)$ be the approximate DtN numbers of the learned infinite elements as in equation [\(2.3\)](#). For positive weights w_ℓ we define the misfit function*

$$(4.1) \quad J(A, B) = \frac{1}{2} \sum_{\ell} |w_{\ell}(\mathit{dtn}(\lambda_{\ell}) - \mathit{dtn}(\lambda_{\ell}))|^2.$$

The minimization problem is to find $A, B \in \mathbb{C}^{(N+1) \times (N+1)}$ so that

$$(4.2) \quad A, B \in \underset{A, B \in \mathbb{C}^{(N+1) \times (N+1)}}{\operatorname{argmin}} J(A, B).$$

Some remarks about this minimization problem are given below.

- In applications the transparent boundary condition is usually combined with a finite element discretization of an interior problem. The weights w_ℓ in the misfit function [\(4.1\)](#) determine how accurate the corresponding dtn -function will be fitted for which modes. As solutions to PDEs with constant or analytic coefficients are analytic, the coefficients of these modes usually decay exponentially. Therefore, also the weights should asymptotically decay exponentially. However, to achieve optimal results the profile pertaining the propagating modes should be chosen with some care. Appropriate choices are discussed when considering example problems in [section 6](#).
- The choice of the objective function [\(4.1\)](#) is motivated by our demand to obtain an optimal approximation of the DtN map in a reasonable sense. Approaches which are to some extent related have been pursued before. For example, in [\[19\]](#) high-order *local* non-reflecting boundary conditions are constructed based on the requirement to provide L^2 best approximations of the DtN map for smooth functions which can be realized via auxiliary variables [\[20\]](#). Here we do not confine ourselves to local approximations, and instead of using the L^2 norm, the approach considered here is based on the natural norm of \mathcal{DtN} as a continuous linear operator from $H^s(\Gamma)$, $s \geq 1/2$ to $H^{-1/2}(\Gamma)$. The attentive reader may have noticed that this is not completely true since the operator norm would be bounded by $\sup_{\ell} |\mathit{dtn}(\lambda_{\ell}) - \mathit{dtn}(\lambda_{\ell})|$ while a weighted ℓ^2 norm is considered in the objective function. This choice is made for ease of implementation and justified for smooth solutions for which it suffices to control a finite number of modes so that equivalence of norms holds true.

- Note that the misfit function is formulated in terms of the continuous eigenvalues λ_ℓ . The discrete eigenvalues and eigenvectors are not needed.
- We had good success with using trust region methods for solving the nonlinear least squares problem (4.2). Specifically, we utilize the Levenberg-Marquardt algorithm as implemented in the **Ceres-solver** [2]. Implementational details are described in [Appendix B](#).

4.2. Reduced ansatz. For dense matrices A and B the number of nonzero entries of the tensor product system $A \otimes M + B \otimes K$ grows quadratically with N . To improve efficiency and to reduce the number of free parameters it is therefore desirable to sparsify A and B . The next step is to identify which entries are dispensable. To this end, let us assume that

$$(4.3) \quad (B_{EE})^{-1}A_{EE} \text{ is diagonalizable,}$$

that is, there exists a diagonal matrix D and an invertible matrix P such that $(B_{EE})^{-1}A_{EE} = PDP^{-1}$ (see also [Remark 4.2](#)). Then

$$(A_{EE} + \lambda B_{EE})^{-1} = P(D + \lambda I)^{-1}(B_{EE}P)^{-1}$$

holds. Inserting this identity into (2.3) yields that the reduced ansatz

$$A = \begin{bmatrix} A_{00} & A_{01} & \cdots & \cdots & A_{0N} \\ A_{10} & \ddots & & \mathbf{0} & \\ \vdots & & \ddots & & \\ \vdots & \mathbf{0} & & \ddots & \\ A_{N0} & & & & A_{NN} \end{bmatrix}, \quad B = \begin{bmatrix} B_{00} & B_{01} & \cdots & \cdots & B_{0N} \\ 1 & 1 & & \mathbf{0} & \\ \vdots & & \ddots & & \\ \vdots & \mathbf{0} & & \ddots & \\ 1 & & & & 1 \end{bmatrix}$$

leads to the same dtn function as the approach with dense matrices A and B . The resulting system $A \otimes M + B \otimes K$ will be much sparser though, and the number of free parameters grows only linearly with N .

In the reduced ansatz dtn is a rational function which is asymptotically linear and has a finite number of simple poles. This can be seen from the formula

$$(4.4) \quad \text{dtn}(\lambda) = A_{00} + \lambda B_{00} - \sum_{j=1}^N \frac{(A_{0j} + \lambda B_{0j})(A_{j0} + \lambda)}{A_{jj} + \lambda}.$$

The second term is a rational function with simple poles at

$$(4.5) \quad \lambda_j^*(N) = -A_{j,j}, \quad j = 1, \dots, N.$$

This means that the diagonal entries of $-A$ correspond to simple poles of the rational approximation. Thus, by optimizing the matrices we optimize the poles at the same time.

Remark 4.2 (Assumption (4.3)). Poles with higher multiplicities are excluded by assumption (4.3) and are consequently not covered by the reduced ansatz. If this assumption breaks down, then the ansatz using dense matrices is more general as it would allow for higher multiplicities and may lead to a better approximation of dtn by dtn. However, below, in [subsection 4.4](#) we show that the reduced ansatz is still sufficient to guarantee exponential convergence rates on finite intervals. Additionally, all dtn functions which we investigated so far had only simple poles which renders an ansatz for dtn of the form (4.4) very natural.

4.3. Pole structure. To justify the previously introduced reduction the following numerical experiment is considered. The analytic DtN numbers for the Helmholtz equation in [Example 3.1](#) with $d = 2$ are obtained by evaluating the function given in [\(3.11\)](#) at $\lambda = \lambda_\ell = (\ell/a)^2$. These numbers $\text{dtn}(\lambda_\ell)$ with $a = 1$ and $k = 16$ are used as reference values for solving the minimization problem [\(4.1\)-\(4.2\)](#). If the diagonalization is justified then the reduced ansatz should lead to the same results as the dense approach. For this test case exponentially decaying weights $w_\ell \sim \exp(-2\ell/3)$ are chosen. In [Figure 3a](#) the relative errors

$$\frac{|\text{dtn}(\lambda_\ell) - \text{dtn}(\lambda_\ell)|}{|\text{dtn}(\lambda_\ell)|}$$

for the dense and reduced ansatz are compared for $N \in \{0, 2, 4, 6\}$. Apparently, both approaches yield the same results. Since the learned DtN based on the reduced ansatz offers the same accuracy as the dense approach and results additionally into a sparser exterior system it is in practice the method of choice.

The poles for the numerical experiment from the previous paragraph are shown in [Figure 3b](#). They are located in the quadrant $\{z \in \mathbb{C} \mid \Re(z) > 0, \Im(z) > 0\}$. Additionally, the exact poles of the meromorphic extension of dtn^{hom} are displayed. [Figure 3b](#) suggests that some of the learned poles seem to converge to the exact poles. In particular, the analytic and learned poles with the smallest imaginary part are placed at the same location for $N \in \{4, 5, 6\}$.

We point out that simply using the N poles of dtn^{hom} with smallest imaginary parts to define dtn yields a much worse approximation in this example.

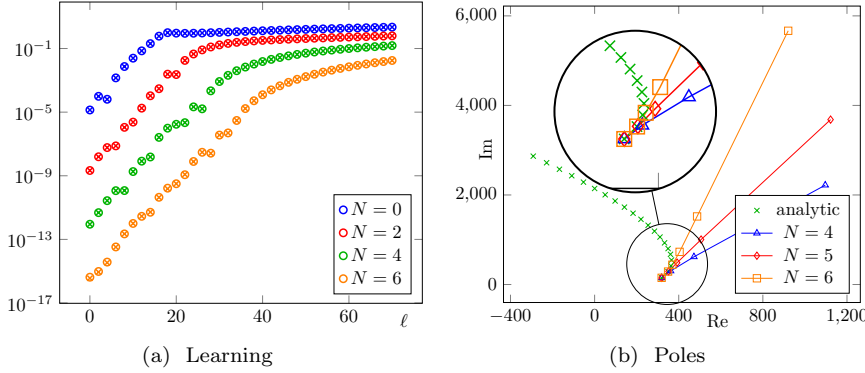


FIG. 3. Left: Comparison of the relative error $|\text{dtn}(\lambda_\ell) - \text{dtn}(\lambda_\ell)|/|\text{dtn}(\lambda_\ell)|$ in terms of N for solving the minimization problem for the analytic DtN numbers from [\(3.11\)](#). The circles ‘o’ display the results for the dense ansatz of A and B while the crosses ‘x’ belong to the reduced ansatz. Note that all crosses lie perfectly inside the circles. For better illustration only results for even ℓ are shown. Right: Poles for the diagonal ansatz when learning the DtN numbers from [\(3.11\)](#).

4.4. Convergence. The results shown in [Figure 3a](#) suggest that the approximation quality of dtn improves exponentially with the number of infinite element DOFs N . A rigorous proof of this observation could serve as the basis of an error analysis for finite element simulations with learned infinite elements as transparent boundary condition. However, note that no uniform rates in λ for $\sup_{\lambda \geq 0} |\text{dtn}(\lambda) - \text{dtn}(\lambda)|$ can be expected due to the nontrivial asymptotic behavior of $\text{dtn}(\lambda)$ at infinity. Hence, smoothness of the solution has to be exploited in order to reduce the

approximation problem to finite intervals. Here, exponential convergence rates can be established as outlined below.

The approximation space of learned infinite elements contains in particular functions of the form

$$r_n(\lambda) = \sum_{j=1}^n \frac{1}{\lambda - a_j}, \quad \{a_j\} \subset \mathbb{C},$$

which are known in the literature as simple partial fractions (SPFs). It seems that the approximation properties of SPFs have been investigated mostly in the Russian literature. A recent overview is given in [13]. For our purpose the following result derived in [31] is of major importance. Let K be a compact and rectifiable set of the complex plane and f be analytic at its interior points and continuous on the closure. Denote by SR_n the set of SPFs with degree at most n , the supremum norm on K by $\|\cdot\|_{C(K)}$, and the best uniform approximation on K by

$$\rho_n(f, K) := \inf\{\|f - r_n\|_{C(K)} \mid r_n \in SR_n\}.$$

Denote the same quantity for polynomials $\mathbb{P}_{\mathbb{C}}^n$ of degree at most n by

$$E_n(f, K) := \inf\{\|f - r_n\|_{C(K)} \mid r_n \in \mathbb{P}_{\mathbb{C}}^n\}.$$

Then the weak equivalence

$$(4.6) \quad \rho_{n+1}(f, K) \simeq E_n\left(fe^{\theta(f;b,\cdot)}, K\right)$$

between the best approximation error with polynomials and SPFs holds. Here, for a fixed $b \in K$ the function $\theta(f; b, z) = \int_b^z f(t) dt$ is an antiderivative for f taken along a path contained in K with length smaller than some $\tilde{d} > 0$. The notation \simeq means bounded from above and below by a constant which depends (exponentially) on $\|f\|_{C(K)}$ and \tilde{d} .

It remains to specialize this result to our setting and combine it with classical approximation theory for polynomials. To this end, it is important to note that $\lambda \mapsto dtn(\lambda)$ is smooth on $(0, \infty)$, cf. [subsection 3.3](#). This allows to invoke standard results (e.g. Jackson's theorem) to bound the best approximation error with polynomials appearing in (4.6). Even the use of approximation results for analytic functions on subsets of the complex plane is possible (see e.g. chapter 4.5 of [41]) thanks to the analytic extensions of dtn as discussed in [section 3](#). Exponential convergence in N on finite intervals follows. The derivation of explicit error estimates is planned to be the subject of another publication.

5. Tensor product discretizations and infinite elements. In this section we will relate the tensor product ansatz (2.2), which is the starting point for our learned infinite elements, to existing successful transparent boundary condition, in particular infinite elements and demonstrate that the algebraic structure of (2.2) is shared by these methods.

5.1. Tensor product infinite elements. Infinite elements can be regarded as an extension of finite elements to infinite domains. Recall that a finite element is a triple (T, Π, Σ) consisting of a closed bounded domain T with sufficiently regular boundary, a finite dimensional space Π of functions defined on T , and a set Σ of

linearly independent functionals with $\#(\Sigma) = \dim \Pi$. Infinite elements relax the first condition by allowing infinite domains. We say that an infinite element E is the tensor product of a finite element $(T_\Gamma, \Pi_\Gamma, \Sigma_\Gamma)$ on Γ and another finite element (T_r, Π_r, Σ_r) if $E = (T_r \times T_\Gamma, \Pi_r \otimes \Pi_\Gamma, \Sigma_r \otimes \Sigma_\Gamma)$.

If tensor product infinite elements of the same type, say with $\Pi_r = \text{span}\{g_0, \dots, g_N\}$ are attached to each patch of the finite element grid on the coupling boundary Γ , then a basis of global shape functions corresponding to the exterior domain is also of tensor product structure:

$$(5.1) \quad \psi_\alpha(r, \hat{x}) = g_\mu(r) \phi_i(\hat{x}), \quad \alpha = (i, \mu) \in \{0, \dots, N\} \times \{1, \dots, n_\Gamma\}$$

Here as in [section 2](#) ϕ_i are finite element basis functions on the coupling interface Γ . To mold the arising linear systems into a convenient form a special partition of the DOFs is employed. In the following, (u_α) is considered as a block-vector where each block contains all unknowns on the coupling interface labeled by $i = 0, 1, \dots, n_\Gamma$ for fixed μ :

$$(5.2) \quad (\underline{u}_\alpha) = \left(\overbrace{(\underline{u}_{\cdot, \mu=0})}^{\Gamma\text{-DOF}}, \overbrace{(\underline{u}_{\cdot, \mu=1}), \dots, (\underline{u}_{\cdot, \mu=N})}^{E\text{-DOF}} \right)^\top = (\underline{u}_\Gamma, \underline{u}_E)^\top.$$

Additionally, in order to obtain a convenient form of DtN, it is assumed that the $\mu = 0$ -DOF of the infinite elements is associated with the coupling interface (label Γ) while the $\mu > 0$ -DOFs belong to the exterior (label E).

For a variational formulation reflecting the structure (3.4) of the exterior PDE, such an ordering of the DOF leads to the tensor product structure (2.2). Rather than formalizing this statement, we will illustrate it at the example of perfectly matched layers, which will also serve as a reference in our numerical examples. We emphasize that perfectly matched layers are typically not derived as infinite elements, but tensor product discretizations of perfectly matched layers may be interpreted as infinite elements as discussed below.

5.2. Perfectly Matched Layers. Perfectly Matched Layers (PML) as first introduced in [7] implement artificial absorbing layers next to the boundary of the exterior domain and truncate the exterior domain rendering it bounded. In our setting of a separable geometry (cf. also [11] for the PML formulation in curvilinear coordinates) the crucial idea can be described as stretching of the r coordinate into the complex plane by means of a transformation

$$(5.3) \quad \tilde{r}(r) = r + \int_a^r i\sigma(t)dt,$$

where σ is a positive function describing unisotropic absorption in propagation direction. This requires the coefficients involved in \mathcal{A} and \mathcal{B} to have analytic extensions. In the new \tilde{r} coordinates radiating solutions decay exponentially whereas incoming solutions grow exponentially. Therefore, the computational domain can be truncated by restricting \tilde{r} to an interval $[a, R]$.

Assume that $|\det \Psi(r, \hat{x})| = r^m$, $(\mathcal{B}u)(r) = \varphi_1(r)u(r)$, and \mathcal{A} is in divergence form $(\mathcal{A}u)(r) = r^{-m} \partial_r (r^m \phi_3(r) \partial_r u(r)) + \varphi_2(r)u(r)$ and with analytic functions φ_j . This covers Examples 3.1 and 3.3. Set $\tilde{u}(r, \hat{x}) := u(\Psi(\tilde{r}(r), \hat{x}))$ and analogously for analytic, rapidly decaying test functions v . Since $(\partial_r u)(\Psi(\tilde{r}(r), \hat{x})) = \partial_r \tilde{u}(r, \hat{x}) / \tilde{r}'(r)$ by the chain rule, a contour deformation in the standard variational formulation of

(3.2) and truncation of the interval $[a, \infty)$ to $[a, \eta]$ leads to the variational formulation

$$\int_{\Gamma} \int_a^{\eta} \left[\tilde{\varphi}_3 \frac{\partial_r \tilde{u} \partial_r \tilde{v}}{(\tilde{r}')^2} + \tilde{\varphi}_2 \tilde{u} \tilde{v} + \tilde{\varphi}_1 \nabla_{\hat{x}} \tilde{u} \cdot \nabla_{\hat{x}} \tilde{v} \right] \tilde{r}^m \tilde{r}' dr d\hat{x} = 0$$

with $\tilde{\varphi}_j := \varphi \circ \tilde{r}$, the unknown function \tilde{u} satisfying $\tilde{u}(a, \cdot) = u_0$ and test functions \tilde{v} satisfying $\tilde{v}(a, \cdot) = 0$.

It is natural – although not necessary – to use a tensor product infinite elements for the discretization of the PML layer $[a, \eta] \times \Gamma$. In this case one may formally combine all one-dimensional finite elements in propagation direction r to one infinite element. This shows that tensor product PMLs may also be interpreted as infinite elements. Expanding \tilde{u} and \tilde{v} in the basis (5.1) leads to a system of equations of the form (2.2) with the matrices

$$(5.4) \quad A_{\mu\nu} = \int_a^{\eta} \left[\tilde{\varphi}_3 \frac{\partial_r g_{\mu} \partial_r g_{\nu}}{(\tilde{r}')^2} + \tilde{\varphi}_2 g_{\mu} g_{\nu} \right] \tilde{r}^m \tilde{r}' dr \quad \text{and} \quad B_{\mu\nu} = \int_a^{\eta} \tilde{\varphi}_1 g_{\mu} g_{\nu} \tilde{r}^m \tilde{r}' dr.$$

5.3. Other infinite elements. Typically, there is no straightforward variational formulation of time harmonic wave equations in exterior domains. The reasons are that neither the solutions themselves nor their gradients are square integrable and that the radiation condition is difficult to incorporate. Therefore, whereas finite elements specify a generic finite dimensional function space for a given mesh, infinite elements are usually intimately linked to a specific PDE and/or a type of variational formulation. In classical infinite elements for the Helmholtz equation, shape functions are chosen according to asymptotic expansions of the exterior solution, and solution and test function spaces are equipped with different weights (cf. [14]). As discussed above, PMLs use standard shape functions, but a transformation of the exterior PDE or its variational formulation. In a similar vein, Hardy space infinite elements (HSIE) [28] are based on a transformation of the PDE to a Hardy space in the propagation direction in order to incorporate the radiation condition. The matrices A and B are obtained by a Galerkin approximation of the transformed variational formulation with respect to a basis of the Hardy space.

$$\begin{bmatrix} A_{\Gamma\Gamma} & A_{\Gamma E} \\ A_{E\Gamma} & A_{EE} \end{bmatrix} \otimes M + \begin{bmatrix} B_{\Gamma\Gamma} & B_{\Gamma E} \\ B_{E\Gamma} & B_{EE} \end{bmatrix} \otimes K$$

Reduction:

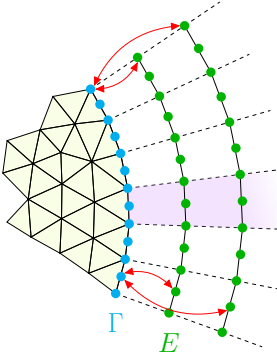
$$A_{EE} = \text{diag}(A_{11}, \dots, A_{NN}), \quad B_{EE} = \text{Id}$$


FIG. 4. Schematic illustration of learned infinite elements. The violet region indicates one such infinite element. The first infinite element DOFs lie on the transparent boundary Γ and are associated with the matrices $A_{\Gamma\Gamma}$ and $B_{\Gamma\Gamma}$. Additional infinite element DOFs in the exterior E are tensorized with copies of the FEM discretization of $(\text{Id}_{\Gamma}, -\Delta_{\Gamma})$ on Γ . The reduction step of subsection 4.3 decouples exterior DOFs (of different rings) from each other. The exterior E couples to Γ (and thereby to Ω_{int}) by means of $A_{\Gamma E}$, $B_{\Gamma E}$, and $A_{E\Gamma}$, $B_{E\Gamma}$.

5.4. Learned infinite elements. In contrast to classical infinite elements where the matrices A and B in (2.2) are computed from some discretization of the (possibly

transformed) exterior PDE, with learned infinite elements we only access the exterior PDE via the associated Dirichlet-to-Neumann map \mathcal{DtN} . Since the matrices A and B will be learned from \mathcal{DtN} , the choice of the element (T_r, Π_r, Σ_r) is irrelevant, only the dimension of Π_r counts. We will simply choose T_r as discrete set $T_N := \{0, 1, \dots, N\}$. With $\Pi_N := \mathbb{C}^{T_N}$ and the canonical dual basis $\Sigma_N := \{F_0, \dots, F_N\}$ given by $F_j(g) := g(j)$ for $g \in \Pi_N$ and $j \in T_N$, tensor product infinite elements of order $N \in \mathbb{N} \cup \{0\}$ are defined by

$$(T_N \times T_\Gamma, \Pi_N \otimes \Pi_\Gamma, \Sigma_N \otimes \Sigma_\Gamma)$$

for finite elements $(T_\Gamma, \Pi_\Gamma, \Sigma_\Gamma)$ on Γ . This is illustrated in [Figure 4](#). Before the learning step discussed in [section 4](#) they are more generic, and after the learning step they are more specific than classical infinite elements. Moreover, as learned infinite elements are based on the same underlying algebraic structure [\(2.2\)](#) as many other transparent boundary conditions like tensor-product PMLs well-established methods for solving the linear systems can be applied.

6. Numerical results. This section presents a variety of numerical experiments to illustrate the performance of learned infinite elements. Firstly, problems with a homogeneous exterior domain are considered to facilitate a comparison with other transparent boundary conditions. Afterwards, increasingly more inhomogeneous exterior domains are tackled leading finally to a realistic test case for the solar atmosphere. The reduced ansatz for the learned infinite element matrices is used by default. All experiments involving finite elements have been implemented using the library `Netgen/NGSolve`, see [\[36, 37\]](#). The order of the finite element discretization is denoted by p . A Docker image providing all software, data and instructions to reproduce the experiments is available at [\[27\]](#). For getting a quick first impression of the new method we also offer a couple of notebooks [\[26\]](#) which can be run live in the browser.

6.1. Scattering of plane wave from a disk. Consider a plane wave $g = \exp(ikx)$ which is incident on a disk with radius $R_s = 1/2$. For sound-soft scattering, i.e. $u = g$ at $r = R_s$, the solution of the Helmholtz equation is given by (see the appendix for derivation)

$$(6.1) \quad u(r, \varphi) = \frac{H_0^{(1)}(kr)}{H_0^{(1)}(kR_s)} J_0(kR_s) + \sum_{\ell=1}^{\infty} \frac{H_\ell^{(1)}(kr)}{H_\ell^{(1)}(kR_s)} 2i^\ell J_\ell(kR_s) \cos(\ell\varphi).$$

Here J_n and $H_n^{(1)}$ denote the Bessel and Hankel function of the first kind of order n respectively.

The problem is discretized on an annulus $\Omega_{\text{int}} = \{x \in \mathbb{R}^2 \mid R_s \leq \|x\| \leq a\}$ using the Dirichlet boundary condition at $r = R_s$ and learned infinite elements at $r = a$. The resolution is increased by raising the polynomial degree while the mesh remains fixed. As discussed in [subsection 4.1](#) the weights in the misfit function should reflect the regularity of the expected solution. This motivates the choice $w_\ell \sim |H_\ell^{(1)}(ka)/H_\ell^{(1)}(k\tilde{r}(k))|$, where $\tilde{r}(k) = \min\{R_s, R_s \cdot k/16\} \leq R_s$ describes the radius of the smallest ball into which the solution is expected to extend analytically into the scatterer.

The relative error on Ω_{int} for increasing number N of infinite element DOFs is shown in [Figure 5](#). The convergence in N is extremely fast. For $p = 6$ and $k = 16$ the spatial accuracy is reached with only $N = 3$ DOFs as [Figure 5a](#) shows. [Figure 5b](#) demonstrates that the method delivers good results for a wide range of wavenumbers.

The performance of most transparent boundary conditions is known to depend on the number of wavelength that fit between scatterer and the coupling boundary. The further away the coupling boundary the more the highly oscillatory components of the solution have already decayed when reaching it. Hence, it suffices to focus attention only on a couple of dtn numbers associated with slowly propagating modes, i.e. to fit $|\hat{dtn}^{\text{hom}}(\lambda_\ell) - \text{dtn}(\lambda_\ell)|$ for small ℓ well, to obtain an accurate solution when $|a - R_s|$ is large. In this regard, the choice $|a - R_s| = 1/2$ considered for the previous experiment is rather generous. Therefore, an additional experiment is performed in which the coupling boundary is moved progressively closer to the scatterer. To this end, $R_s = 1/2$ is fixed and a is decreased so that $|a - R_s| \in [1/2, 1/4, 1/8, 1/16]$. The results for $k = 16$ are displayed in Figure 6. As expected, the convergence rate of the relative error slows down as the coupling boundary approaches the scatterer. Nevertheless, the convergence is still exponential. Figure 6b also shows that the weighted uniform error of the dtn modes is proportional to the relative L^2 -error. This provides an a priori estimate on the accuracy of learned IEs in the sense that the error stemming from the DtN approximation can be measured directly after the minimization problem (4.2) has been solved.

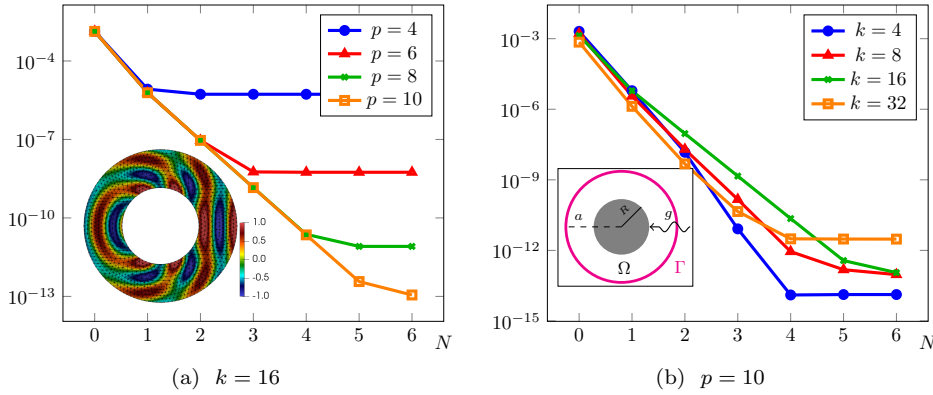


FIG. 5. Comparison of relative error $\|u - u_h\|_{L^2(\Omega_{\text{int}})} / \|u\|_{L^2(\Omega_{\text{int}})}$ for the scattering of a plane wave from a disk. Additionally, the real part of the reference solution for $k = 16$ is shown in the left figure.

6.2. Point source inside unit disk. The fundamental solution $\Phi(x, y) = (i/4)H_0^{(1)}(k\|x - y\|)$ fulfills

$$-\Delta_x \Phi(x, y) - k^2 \Phi(x, y) = \delta(x - y) := \delta_y(x),$$

where δ_y is the Dirac distribution at $y \in \mathbb{R}^2$. The point source y is placed inside a disk with radius $a = 1$. In this example $\nabla_x \Phi(x, y) \cdot \nu(x)$ is directly used as Neumann data for the exterior problem realized e.g. by the learned infinite elements. In particular, there is no interior discretization. The quality of the solution is assessed by measuring the relative L^2 -error in the Dirichlet data on Γ . The difficulty of the problem increases with shrinking distance of the source to the boundary as this adds more significant modes to the solution. The weights for the minimization problem are chosen accordingly as $w_\ell \sim |H_\ell^{(1)}(ka)/H_\ell^{(1)}(k\|y\|)|$. To investigate the influence on the transparent boundary condition the source positions $y = (0.5, 0.0)$ and $y = (0.95, 0.0)$ are considered in the experiments.

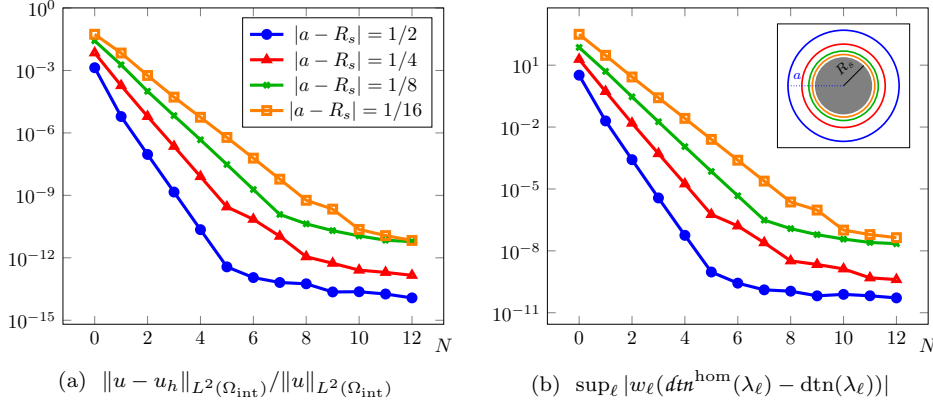


FIG. 6. Influence of the distance $|a - R_s|$ between coupling boundary and scatterer on the performance of learned IEs for $k = 16$ and $p = 12$. Relative L^2 -error on Ω_{int} on the left and weighted uniform error of the dtn modes on the right.

To evaluate the performance of learned infinite elements a comparison with other transparent boundary conditions is presented. For the experiments below a quadratic absorption coefficient $\sigma(t) = (C/k)(1/(\eta - a))((t - a)/(\eta - a))^2$ was used in (5.3). The parameters $C = 40$ and $\eta - a = 0.02$ have been found to yield good results. The implementation uses finite elements of order four with uniform mesh refinements.

Tuning of the PML and discretization parameters in this approach is tedious and may lead to suboptimal results. A better strategy has been proposed in [9]. Following [11] the medium parameter σ_0 in $\sigma(t) = \sigma_0((r - a)/(\eta - a))^m$, $m \in \mathbb{N}$ and the thickness $\eta - a$ in the complex stretching of the PML are determined through an a posteriori error analysis. This is achieved by splitting the error into a finite element discretization error and a term describing the modeling error introduced by the PML (see Theorem 3.1. in [9]). The contribution from the PML decreases with the exponentially decaying factor

$$\exp\left(-k\Im(\tilde{\eta})\left(1 - \frac{a^2}{|\tilde{\eta}|^2}\right)^{1/2}\right), \quad \tilde{\eta} = \eta + i\frac{\sigma_0}{m+1}(\eta - a).$$

By choosing $m = 2$, $\sigma_0 = 4.5$, and $\eta = 2.5$ the PML error is of the order of the machine precision for the considered example. With the PML parameters being fixed an adaptive mesh refinement strategy based on a standard residual error estimator is employed to reduce the discretization error. Note that this leads to an unstructured mesh. In particular this method is not of the tensor product form (2.2). For the experiments presented here finite elements of order six have been chosen.

As a last candidate we consider the Hardy space infinite element method (HSIE), cf. subsection 5.3. This method has a parameter which is usually called κ_0 . For the experiments below $\kappa_0 = ak$ was used for $y = (0.5, 0)$ while a larger value of $\kappa_0 = 3ak$ turned out to be beneficial for $y = (0.95, 0)$.

In Figure 7 the different methods are compared in terms of the number of DOFs ('ndof') and number of nonzero entries ('nze') of the resulting linear system.

- The lower panel displays the results for a source far away from the boundary. In this case both methods based on infinite elements outperform the PML approaches. Although the HSIE already works very well for this problem,

the learned approach yields a further improvement. The reduced ansatz for the infinite elements matrices ('Learned reduced') results in a sparser system matrix but makes the optimization problem a bit harder to solve. As a result, it may happen that the minimization gets stuck in a local minimum or makes slower progress compared to the dense ansatz. However, so far this has only been observed in the very high accuracy range. In Figure 7c and Figure 7d this occurred for relative accuracy better than 10^{-12} .

- The upper panel gives the results for the source close to the boundary. Here, the performance of the HSIE degrades strongly. Both PML approaches perform better in terms of nonzero entries of the linear system. Among the PML methods, the adaptive discretization achieves substantially better results than the tensor product PML. In particular, it leads to very sparse matrices. Still, the learned infinite elements are able to improve on this.

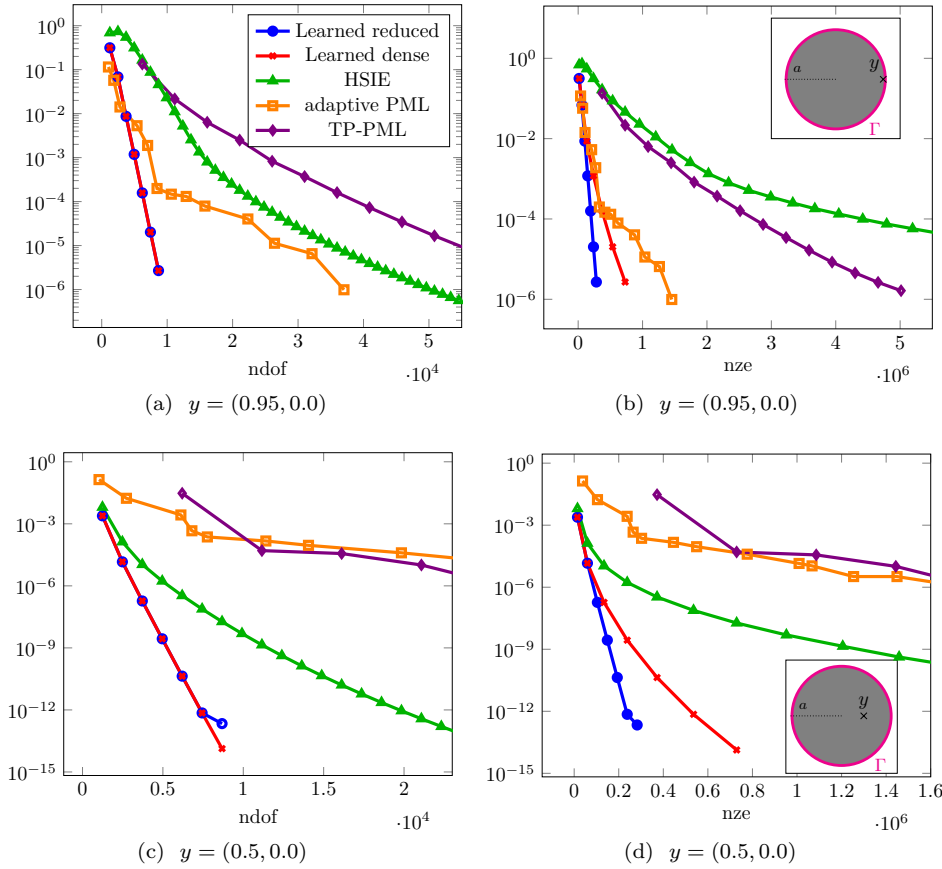


FIG. 7. Comparison of relative error $\|u - u_h\|_{L^2(\Gamma)} / \|u\|_{L^2(\Gamma)}$ for the point source inside the unit disk at position y with $k = 16$.

6.3. Jump in exterior wavenumber. For the numerical experiments $a = 1$, $R_J = 2$ and $k_I = 16$ are chosen in Example 3.2. In Figure 8a and Figure 8c the approximation $\text{dtn}(\lambda)$ obtained with the reduced ansatz (4.4) for different N is shown. While Figure 8a shows the case $k_\infty = k_I = 16$ in which there is no jump and the

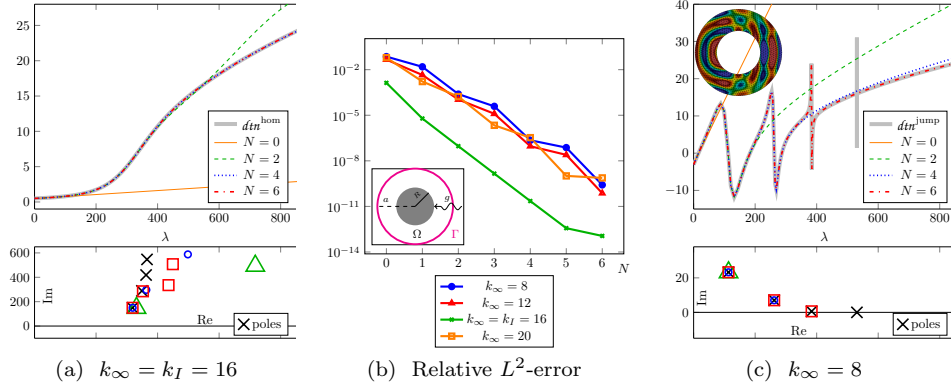


FIG. 8. Approximation results for the real part of dtn^{jump} from Example 3.2 with a discontinuous exterior wavenumber jumping from $k_I = 16$ to $k_\infty = 8$ shown in Figure 8c compared to the dtn^{hom} function of the homogeneous medium, which is recovered for the case $k_I = k_\infty = 16$, in Figure 8a. In the lower panel we also compare the poles of dtn (black crosses) to the poles of dtn (colors according to legend). Only the poles of dtn close to the real axis are displayed. The relative L^2 -error for the scattering of a plane wave is shown in the central figure.

dtn^{hom} function of the homogeneous medium is recovered, Figure 8c displays a case in which the wavenumber jumps drastically. Additionally, the poles of the meromorphic extension of dtn and the learned poles (see (4.5)) are displayed. The approximation results for the case $k_\infty = 8$ shown in Figure 8c are astonishing. The rapid improvement as N increases can be explained by considering the positioning of the learned poles. For $N = 2$ the optimization routine has placed one of the learned poles at the position of the first exact pole. This captures the first peak of dtn^{jump} . For $N = 4$ the next pole has been fitted and accordingly the next peak is covered by the approximant. It is remarkable that for $N = 6$ the peak can be captured accurately even though it is not resolved by the sampling of the λ -axis in the minimization problem. Similar results shown in the appendix are obtained for $k_\infty = 12$ and $k_\infty = 20$. This clearly demonstrates the benefits of using rational functions for approximating the dtn .

In analogy to subsection 6.1 we consider the scattering of a plane wave from a disk with radius $R_s = 1/2$. An analytic reference solution for this problem, displayed in Figure 8c for $k_\infty = 8$, is derived in the appendix. For the case $k_\infty = k_I = k$ it reduces to the solution (6.1) for the homogeneous problem, whose real part was shown in Figure 5a. The weights are chosen as $w_\ell \sim |u_\ell(a)/u_\ell(\tilde{r}(k_I))|$, where $u_\ell(r) = A_\ell J_\ell(k_I r) + B_\ell Y_\ell(k_I r)$ is the solution of the radial equation for $r < R_J$ and $\tilde{r}(k_I)$ is as in subsection 6.1. The relative L^2 -error on the computational domain Ω_{int} is shown in Figure 8b for different k_∞ . Although the error is a bit larger when a jump actually occurs, i.e. $k_\infty \neq k_I$, the convergence is nevertheless exponential.

6.4. Waveguide. In this section we consider the waveguide introduced in Example 3.3. Setting $\tilde{\Gamma} = [0, \pi]$ and letting the waveguide start at the origin the solution shall be computed in $\Omega_{\text{int}} = [0, a) \times \tilde{\Gamma}$. The geometry is sketched in Figure 1c. It is convenient to choose Dirichlet boundary conditions on $\partial\Omega_{\text{int}} \setminus (\{a\} \times \tilde{\Gamma})$ so that the exact solution is given by

$$u = \sum_{\ell=0}^L \sin(y\sqrt{\lambda_\ell}) \exp(ix\sqrt{k^2 - \lambda_\ell}),$$

for $\lambda_\ell = \ell^2$. For the numerical experiment the parameters $a = 2\pi$, $k = 16.5$ and $L = 33$ are chosen. Note that (3.14) holds. The weights are chosen to cover all propagating waveguide modes equally well and emulate the decay of the evanescent modes, i.e. $w_\ell \sim 1$ for $\lambda_\ell \leq k^2$ and $w_\ell \sim |\exp(ia\sqrt{k^2 - \lambda_\ell})|$ else.

In Figure 9 results for the approximation of $\Im(dtn^{\text{guide}})$ are shown. (Note the $\Re(dtn^{\text{guide}})$ is zero for most relevant modes.) As one might expect, the kink of dtn^{guide} is hardest to resolve. Interestingly, the learned poles are observed to accumulate in the part of the complex plane lying to the right of the kink, which is probably beneficial for approximation. We also note that the approximation at the sample points $dtn^{\text{guide}}(\lambda_\ell)$ is extremely accurate for large N . This can be expected from the paper [35] by Newman who showed that the function $|x|$ can be approximated by rational functions of order N with an error $\leq 3 \exp(-\sqrt{N})$ uniformly on the interval $[-1, 1]$. This (heuristically) explains this type of fast convergence of the relative L^2 -error that can be observed in Figure 9b.

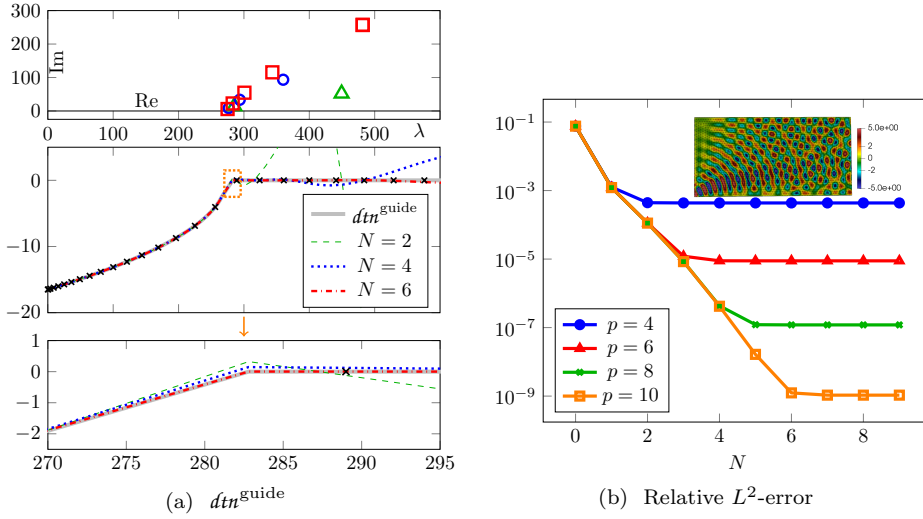


FIG. 9. Left: Approximation results for imaginary part of dtn^{guide} with $k = 16.5$. The sample points $dtn^{\text{guide}}(\lambda_\ell)$ are displayed as black crosses. In the topmost plot also some poles of dtn are displayed. Right: Relative L^2 error on Ω_{int} . Additionally, the real part of the reference solution is shown.

6.5. Application to helioseismology. We now proceed to the main application introduced in subsection 3.4 which fueled the development of learned infinite elements, the approximation of the VAL-C model of the solar atmosphere. At first sight it may seem that a full finite element discretization of the thin layer of validity of the VAL-C model colored blue color in 1d, which comprises only 1.3% of the volume of the Sun, costs only negligible additional effort. However, the wavelength $\lambda = 2\pi c/\omega$ decreases significantly close to and above the visible surface of the Sun such that this thin layer contains 2 wavelengths in radial direction at a frequency of 7.0 mHz, compared to 25 wavelengths in the interior. In order to resolve wave oscillations, the local mesh size h should be roughly proportional to the wavelength. Assuming a regular meshes (in the sense that for each finite element domain D the ratio of the largest ball contained in D to the smallest ball containing D is uniformly bounded) with h proportional to λ , the number of elements in the ball of radius r is

proportional to

$$I(r) := \int_{|x|_2 \leq r} \lambda^{-d} dx,$$

in d dimensions. Table 1 displays the ratio between the wavelength to be resolved in a d -dimensional discretization of the Sun up to the photosphere $I(a)$ and a discretization which covers an additional 2300 km of the solar atmosphere $I(R_V)$ corresponding to the domain of the VAL-C model. Whereas in one dimension, the additional effort for discretization of the atmosphere may be regarded as acceptable, in three dimensions such an additional discretization of the atmosphere would at least triple the computational burden. In view of the notoriously challenging linear systems arising from time-harmonic wave equations such an increase must absolutely be avoided.

d	1 (radial symmetry)	2 (axial symmetry)	3 (no symmetry)
$I(R_V)/I(a)$	1.1	1.8	3.2

TABLE 1

Ratio of the numbers of finite elements of regular d -dimensional finite element meshes of the Sun with mesh size proportional to wavelength for different radii R_V and a . a corresponds to the radius of the photosphere (the visible surface of the Sun) whereas $R_V = a + 2300$ km is the outer radius of the domain of validity of the VAL-C model of the solar atmosphere. These numbers demonstrate the necessity of transparent boundary conditions for the solar atmosphere.

Figure 10 shows the approximations $\text{dtn}(\lambda_\ell)$ of $\text{dtn}^{\text{VAL-C}}$ for different N . For efficiency purposes the distance to $\text{dtn}^{\text{VAL-C}}$ has only been minimized at a subset of the continuous eigenvalues $\lambda_\ell = \ell(\ell+1)/a^2$. This sets consists of two parts. The first is an equidistant sampling in ℓ to resolve the general behavior of $\text{dtn}^{\text{VAL-C}}$. The second is a fine sampling near the poles, which is readily obtained by computing the gradient of the array containing the samples of $\text{dtn}^{\text{VAL-C}}$. The weights decay exponentially as $w_\ell \sim \exp(-\ell/800)$.

Using this strategy similar approximation results as for the example from subsection 6.3 are obtained. Adding more infinite element DOFs allows to resolve an increasing number of the narrow turning points of $\text{dtn}^{\text{VAL-C}}$. The behavior of $\text{dtn}^{\text{VAL-C}}$ on the domain of interest is so completely dominated by the closely located poles that $N = 5$ suffices to obtain an excellent approximation.

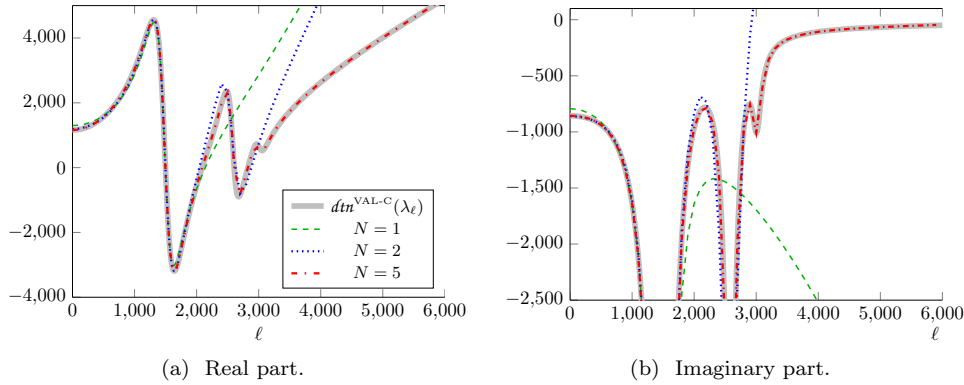


FIG. 10. Approximation results for problem from computational helioseismology at 7.0 mHz.

These results demonstrate that learned infinite elements allow to absorb the atmospheric behavior into a transparent boundary condition with very few DOFs which can be placed directly at the photosphere.

7. Conclusions and outlook. We have proposed a new type of transparent boundary condition in the form of infinite elements. In contrast to traditional methods which involve some explicit modelling of the exterior differential equation, we suggest to obtain a sparse and accurate approximation of the DtN map by ‘learning’ the matrix elements from the DtN map in a preprocessing step. Our analysis applies to separable problems, in particular spherically symmetric problems where the learning process only requires knowledge of the eigenvalues of the continuous DtN map, which are often given analytically, but neither discrete eigenvalues nor discrete eigenvectors are needed. Numerical test show that learned infinite elements for the Helmholtz equation outperform traditional methods such as PMLs both in terms of numbers of degrees of freedom and numbers of nonzero matrix elements. At the same time they are more flexible and applicable to stratified media with non-analytic separable coefficients. A preliminary theoretical analysis suggests exponential convergence with increasing infinite element degrees of freedom. A crucial role is played by the position of singularities of analytic extensions of the ‘eigenvalue function’ of the DtN map, which is initially defined on the spectrum of the Laplace-Beltrami operator of the coupling boundary. This raises new theoretical questions, e.g. concerning potential connections to resonances.

Let us discuss some potential extensions of our approach:

- *Relaxation of the separation assumption (3.4).* This assumption might be replaced by a separation assumption with respect to operator pencils different from the Laplace-Beltrami and the identity operator on the coupling boundary. This could allow to treat systems of PDEs and separation with respect to elliptic coordinates.
- *Infinite elements which work on intervals of wave numbers.* Currently the learned parameters only work for one specific wave number. Therefore, they may hardly be reused. With the proposed extension libraries of optimized coefficients may be set up to allow the use of infinite elements without the need to implement the learning process. Moreover, this may enable the application of infinite elements for the solution of resonance problems.
- *Non-separable differential equations.* To treat such problems one may study learned infinite elements which are not of tensor product form. Here probably it cannot be avoided to set up a discrete DtN map for the learning process in some form, and the number of degrees of freedom would increase significantly. Nevertheless, we see some potential for such approaches, e.g. in the context of domain decomposition methods.

Our favorable numerical results encourage further research on learned infinite elements in these and other directions in order to extend their range of applicability and improve theoretical foundation.

Appendix A. Derivation of dtn and reference solution for jump in exterior wavenumber. For $\nu, a > 0$ consider the problem

$$-\frac{1}{r} \frac{\partial}{\partial r} \left(r \frac{\partial u}{\partial r} \right) + \left(k^2(r) - \frac{\nu^2}{r^2} \right) u = 0 \quad r > a,$$

$$u(a) = 1,$$

with radiation condition at infinity. For some $a \leq R_J < \infty$ let the wavenumber be given by

$$k(r) = \begin{cases} k_I & r < R_J, \\ k_\infty & r > R_J, \end{cases}$$

for some $k_I, k_\infty > 0$.

This problem has the solution

$$u_\nu(r) = \begin{cases} A_\nu J_\nu(k_I r) + B_\nu Y_\nu(k_I r) & r < R_J, \\ C_\nu H_\nu^{(1)}(k_\infty r) & r > R_J, \end{cases}$$

with constants $A_\nu, B_\nu, C_\nu \in \mathbb{C}$ to be determined by the following three constraints:

- Boundary condition at $r = a$

$$(A.1) \quad A_\nu J_\nu(k_I a) + B_\nu Y_\nu(k_I a) = 1.$$

- Continuity at $r = R_J$

$$(A.2) \quad A_\nu J_\nu(k_I R_J) + B_\nu Y_\nu(k_I R_J) - C_\nu H_\nu^{(1)}(k_\infty R_J) = 0.$$

- Continuity of derivative at $r = R_J$

$$(A.3) \quad A_\nu k_I J'_\nu(k_I R_J) + B_\nu k_I Y'_\nu(k_I R_J) - C_\nu k_\infty (H_\nu^{(1)})'(k_\infty R_J) = 0.$$

Solving (A.1) for A_ν gives

$$(A.4) \quad A_\nu = \frac{1 - B_\nu Y_\nu(k_I a)}{J_\nu(k_I a)}.$$

Using this equation to eliminate A_ν from A.2 and (A.3) leads to the linear system

$$\begin{bmatrix} \frac{J_\nu(k_I a)Y_\nu(k_I R_J) - Y_\nu(k_I a)J_\nu(k_I R_J)}{J_\nu(k_I a)} & -H_\nu^{(1)}(k_\infty R_J) \\ \frac{Y'_\nu(k_I R_J)J_\nu(k_I a) - Y_\nu(k_I a)J'_\nu(k_I R_J)}{J_\nu(k_I a)} & -\frac{k_\infty}{k_I} (H_\nu^{(1)})'(k_\infty R_J) \end{bmatrix} \begin{bmatrix} B_\nu \\ C_\nu \end{bmatrix} = \begin{bmatrix} -\frac{J_\nu(k_I R_J)}{J_\nu(k_I a)} \\ -\frac{J'_\nu(k_I R_J)}{J_\nu(k_I a)} \end{bmatrix}.$$

Denote the matrix in this equation as M_ν . We have

$$\begin{aligned} \det(M_\nu) &= -\frac{k_\infty}{k_I} \frac{(H_\nu^{(1)})'(k_\infty R_J)}{J_\nu(k_I a)} [J_\nu(k_I a)Y_\nu(k_I R_J) - Y_\nu(k_I a)J_\nu(k_I R_J)] \\ &\quad + \frac{H_\nu^{(1)}(k_\infty R_J)}{J_\nu(k_I a)} [Y'_\nu(k_I R_J)J_\nu(k_I a) - Y_\nu(k_I a)J'_\nu(k_I R_J)]. \end{aligned}$$

Hence,

$$M_\nu^{-1} = \frac{1}{\det(M_\nu)} \begin{bmatrix} -\frac{k_\infty}{k_I} (H_\nu^{(1)})'(k_\infty R_J) & H_\nu^{(1)}(k_\infty R_J) \\ -\frac{[Y'_\nu(k_I R_J)J_\nu(k_I a) - Y_\nu(k_I a)J'_\nu(k_I R_J)]}{J_\nu(k_I a)} & \frac{J_\nu(k_I a)Y_\nu(k_I R_J) - Y_\nu(k_I a)J_\nu(k_I R_J)}{J_\nu(k_I a)} \end{bmatrix}.$$

The solution of the linear system is given by

$$(A.5) \quad B_\nu = \frac{1}{\det(M_\nu)} \left[\frac{k_\infty}{k_I} (H_\nu^{(1)})'(k_\infty R_J) \frac{J_\nu(k_I R_J)}{J_\nu(k_I a)} - H_\nu^{(1)}(k_\infty R_J) \frac{J'_\nu(k_I R_J)}{J_\nu(k_I a)} \right]$$

and

$$(A.6) \quad C_\nu = \frac{1}{\det(M_\nu)} \left[[Y'_\nu(k_I R_J) J_\nu(k_I a) - Y_\nu(k_I a) J'_\nu(k_I R_J)] \frac{J_\nu(k_I R_J)}{J_\nu(k_I a)^2} \right. \\ \left. - [J_\nu(k_I a) Y_\nu(k_I R_J) - Y_\nu(k_I a) J_\nu(k_I R_J)] \frac{J'_\nu(k_I R_J)}{J_\nu(k_I a)^2} \right].$$

This yields the DtN function

$$(A.7) \quad \zeta(\nu) = -\frac{\partial u_\nu(a)}{\partial r} = -k_I [A_\nu J'_\nu(k_I a) + B_\nu Y'_\nu(k_I a)].$$

A reference solution for a sound-soft scattering problem in the exterior of a disk with radius R_s can easily be obtained from the previous computations. Firstly, the radius of the truncation boundary has to be replaced by the radius of the scatterer, i.e. set $a = R_s$. Assume that a plane wave $g = \exp(ik_I x)$ is incident on the disk. It is well-known that g admits an expansion into orthogonal eigenfunctions of the Laplace-Beltrami operator on the boundary of the scatterer:

$$g = J_0(k_I r) + \sum_{\ell=1}^{\infty} 2i^\ell J_\ell(k_I r) \cos(\ell\varphi),$$

using standard polar coordinates $x = r \cos(\varphi)$ and $y = r \sin(\varphi)$. Hence, by separation of variables the solution is given by

$$(A.8) \quad u(r, \varphi) = u_0(r) J_0(k_I R_s) + \sum_{\ell=1}^{\infty} u_\ell(r) 2i^\ell J_\ell(k_I R_s) \cos(\ell\varphi).$$

A.1. Case of no jump. In the special case

$$(A.9) \quad k_\infty = k_I$$

there is no jump and the following computation shows that the dtn^{hom} function of the homogeneous medium is recovered from (A.7). A straight-forward calculation using (A.9) yields:

$$\det(M_\nu) = \frac{H_\nu^{(1)}(ka)}{J_\nu(ka)} W\{J_\nu(kR_J), Y_\nu(kR_J)\},$$

where $W\{J_\nu(kR_J), Y_\nu(kR_J)\} = J_\nu(kR_J)Y'_\nu(kR_J) - J'_\nu(kR_J)Y_\nu(kR_J)$ is the Wronskian. A similar calculation gives

$$B_\nu = \frac{1}{\det(M_\nu)} \frac{i}{J_\nu(ka)} W\{J_\nu(kR_J), Y_\nu(kR_J)\} = \frac{i}{H_\nu^{(1)}(ka)}.$$

As

$$1 - B_\nu Y_\nu(k_I a) = \frac{J_\nu(ka)}{H_\nu^{(1)}(ka)}$$

it follows from (A.4) that $A_\nu = 1/H_\nu^{(1)}(ka)$. Inserting this into the ansatz for the solution yields $u_\nu(r) = H_\nu^{(1)}(kr)/H_\nu^{(1)}(ka)$ for $r < R_J$ and hence $dtn^{\text{jump}}(\lambda) = dtn^{\text{hom}}(\lambda)$. The reference solution (A.8) then takes the explicit form

$$u(r, \varphi) = \frac{H_0^{(1)}(kr)}{H_0^{(1)}(kR_s)} J_0(kR_s) + \sum_{\ell=1}^{\infty} \frac{H_\ell^{(1)}(kr)}{H_\ell^{(1)}(kR_s)} 2i^\ell J_\ell(kR_s) \cos(\ell\varphi).$$

Appendix B. Implementational details.

In this section some suggestions on how to solve the optimization problem introduced in [subsection 4.1](#) are provided. Although we had good success with the technique outlined below other approaches may be possible. The [Appendix B.1](#) describes how the optimization problem for one specific N is solved and [Appendix B.2](#) then outlines the whole pipeline.

B.1. Solving the optimization problem for a fixed N . The objective function for the minimization problem (4.1)-(4.2) can be written in the form

$$(B.1) \quad J(A, B) = \frac{1}{2} \sum_{\ell} w_{\ell}^2 |f_{\ell}|^2,$$

with $f_{\ell}(A, B) := dtn(\lambda_{\ell}) - \text{dtn}(\lambda_{\ell})$. Here we consider the case where $\text{dtn}(\lambda_{\ell})$ is given by the reduced ansatz (4.4). The general case can be treated along the same lines, yet requires some more computations. The Levenberg-Marquardt algorithm is one of the commonly employed methods for solving non-linear least-squares problems of the form (B.1). Various open source implementations are readily available. These implementations usually require from the user the definition of the parameters, here the entries of A and B to be optimized, the cost functions f_{ℓ} and their gradients with respect to these parameters.

- Only the matrix entries of A and B that are not known a priori should be considered as parameters. So for ansatz (4.4) these are given by

$$\{A_{0j}\}_{j=0}^N \cup \{A_{j0}\}_{j=1}^N \cup \{A_{jj}\}_{j=1}^N \cup \{B_{0j}\}_{j=0}^N.$$

- A potential difficulty could arise from the fact that A and B are complex matrices while the available implementation of the Levenberg-Marquardt algorithm might be limited to real parameters. However, this is easily resolved by splitting into real and imaginary parts

$$A_{nm} = \Re A_{nm} + i \Im A_{nm}$$

and treating $\Re A_{nm}$ and $\Im A_{nm}$ as two separate real parameters. The gradients of the cost functions can easily be calculated analytically:

$$\frac{\partial f_{\ell}}{\partial \Re A_{00}} = -1, \quad \frac{\partial f_{\ell}}{\partial \Re B_{00}} = -\lambda_{\ell}.$$

For $n \geq 1$:

$$\frac{\partial f_{\ell}}{\partial \Re A_{0n}} = \frac{A_{n0} + \lambda_{\ell}}{A_{nn} + \lambda_{\ell}}, \quad \frac{\partial f_{\ell}}{\partial \Re B_{0n}} = \lambda_{\ell} \frac{(A_{n0} + \lambda_{\ell})}{A_{nn} + \lambda_{\ell}}, \quad \frac{\partial f_{\ell}}{\partial \Re A_{n0}} = \frac{A_{0n} + \lambda_{\ell} B_{0n}}{A_{nn} + \lambda_{\ell}},$$

and

$$\frac{\partial f_{\ell}}{\partial \Re A_{nn}} = -\frac{(A_{0n} + \lambda_{\ell} B_{0n})(A_{n0} + \lambda_{\ell})}{(A_{nn} + \lambda_{\ell})^2}.$$

The derivatives with respect to the imaginary part can be obtained from

$$\frac{\partial f_{\ell}}{\partial \Im A_{nm}} = i \frac{\partial f_{\ell}}{\partial \Re A_{nm}}.$$

Please note that the cost functions are complex-valued, so depending on the implementation they may have to be split into real and imaginary parts as well.

B.2. Successive learning. An algorithm for the whole pipeline starting with the computation of $dtn(\lambda_\ell)$ is given in [Algorithm B.1](#).

Algorithm B.1 Successive learning of matrices A and B

```

1: Define  $N_{\max}, L_{\max}$ 
2: for  $\ell = 0 : L_{\max}$  do
3:   Compute  $dtn(\lambda_\ell)$  by solving (3.5a)-(3.5b).
4: end for
5: Initialize  $\tilde{A} \in \mathbb{C}, \tilde{B} \in \mathbb{C}$  randomly.
6: for  $N = 0 : N_{\max}$  do
7:   Obtain  $A, B \in \mathbb{C}^{(N+1) \times (N+1)}$  by solving (B.1) as described in Appendix B.1
     using  $\tilde{A}, \tilde{B}$  as initial guess.
8:   Prepare new initial guess:  $\tilde{A}, \tilde{B} \in \mathbb{C}^{(N+2) \times (N+2)}$ .
9:   Initialize upper block of  $\tilde{A}, \tilde{B}$  by  $A, B$ .
10:  Set  $\tilde{A}_{N+1, N+1}$  to one or a good guess for the poles if available.
11:  Fill  $\tilde{A}_{N+1, 0}, \tilde{A}_{0, N+1}$  and  $\tilde{B}_{0, N+1}$  with small (nonzero) random numbers.
12: end for
13: return Learned matrices  $A, B$  for  $N = 0 : N_{\max}$ .
```

A few additional remarks are given below.

- Often there is an analytic reference solution for $dtn(\lambda_\ell)$ available so that the solution of the ODEs can be skipped.
- The purpose of the loop over N in [Algorithm B.1](#) is to provide a good initial guess for the optimization. Basically, the learned matrices from step N are reused as an initial guess for step $N + 1$. With this technique the learned $dtn(\lambda_\ell)$ -function in step $N + 1$ starts at the value of the minimizer of step N plus the additional term

$$\frac{(\tilde{A}_{0, N+1} + \lambda_\ell \tilde{B}_{0, N+1})(\tilde{A}_{N+1, 0} + \lambda_\ell)}{\tilde{A}_{N+1, N+1} + \lambda_\ell}.$$

In order to prevent the cost function from starting too far away from the minimizer of the previous step this contribution should be small. This is the motivation for filling $\tilde{A}_{N+1, 0}, \tilde{A}_{0, N+1}$ and $\tilde{B}_{0, N+1}$ with small random numbers. These should be nonzero to avoid getting stuck at the minimizer of step N . If a good guess for the poles is available then setting $-\tilde{A}_{N+1, N+1}$ equal to one of these poles can be beneficial.

Appendix C. Additional plots for numerical experiments. [Figure 11](#), [Figure 12](#), [Figure 13](#), [Figure 14](#) and [Table 2](#) show some additional aspects of the numerical experiments described in the main article.

Acknowledgments. This research was funded by the Deutsche Forschungsgemeinschaft (DFG, German Research Foundation) – Project-ID 432680300 – SFB 1456.

J.P. is a member of the International Max Planck Research School for Solar System Science at the University of Göttingen.

Author contributions: T.H. initiated the research on learned infinite elements. All authors designed and performed the research. All implementations and numerical computations were performed by J.P. using the finite element library `Netgen/NGSolve`

N	iter	cost	gradient	time[s]
0	3 / 3	$8.3 \cdot 10^5$ / $8.3 \cdot 10^5$	$7.9 \cdot 10^4$ / $7.9 \cdot 10^4$	$1.8 \cdot 10^{-4}$ / $2.7 \cdot 10^{-4}$
1	34 / 16	$1.3 \cdot 10^2$ / $1.3 \cdot 10^2$	$2.9 \cdot 10^2$ / $1.3 \cdot 10^2$	$8.3 \cdot 10^{-3}$ / $6.3 \cdot 10^{-4}$
2	10 / 16	$6.1 \cdot 10^{-2}$ / $6.1 \cdot 10^{-2}$	$7.5 \cdot 10^{-1}$ / $3.8 \cdot 10^2$	$8.3 \cdot 10^{-3}$ / $1.0 \cdot 10^{-3}$
3	9 / 496	$2.9 \cdot 10^{-5}$ / $2.9 \cdot 10^{-5}$	$1.1 \cdot 10^{-1}$ / $5.8 \cdot 10^0$	$1.7 \cdot 10^{-2}$ / $4.7 \cdot 10^{-2}$
4	12 / 4620	$1.4 \cdot 10^{-8}$ / $1.4 \cdot 10^{-8}$	$4.5 \cdot 10^{-3}$ / $3.5 \cdot 10^{-1}$	$4.9 \cdot 10^{-2}$ / $5.9 \cdot 10^{-1}$
5	20 / 177	$7.2 \cdot 10^{-12}$ / $7.2 \cdot 10^{-12}$	$4.6 \cdot 10^{-3}$ / $3.8 \cdot 10^{-4}$	$1.6 \cdot 10^{-1}$ / $3.0 \cdot 10^{-2}$
6	1491 / 293	$3.7 \cdot 10^{-15}$ / $3.7 \cdot 10^{-15}$	$2.9 \cdot 10^{-3}$ / $3.8 \cdot 10^{-3}$	$2.9 \cdot 10^1$ / $8.1 \cdot 10^{-2}$

TABLE 2

Performance of the Levenberg-Marquardt algorithm for solving the minimization for the Helmholtz equation with $a = 1$ and $k = 16$ from [subsection 4.3](#). Results for the dense / reduced ansatz are given in [red](#) / [blue](#). The cost denotes the value of the objective function at the minimizer, similarly for the gradient.

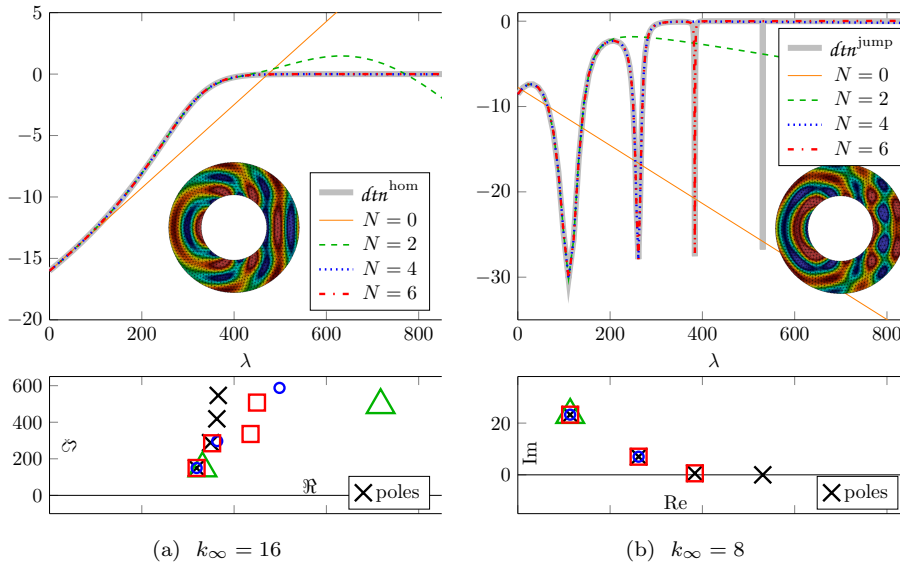


FIG. 11. Approximation results for the imaginary part of dtn belonging to a discontinuous exterior wavespeed which jumps from $k_I = 16$ to k_∞ . In the lower panel we also compare the poles of dtn (black crosses) with the poles of dtn (color according to legend). Only the poles of dtn close to the real axis are displayed.

and the Levenberg-Marquardt algorithm from the **Ceres-solver**. J.P. also conceived [subsection 4.4](#) and drafted the paper. All authors contributed to the final manuscript.

REFERENCES

- [1] A. D. AGALTSOV, T. HOHAGE, AND R. G. NOVIKOV, *Monochromatic identities for the Green function and uniqueness results for passive imaging*, SIAM J. Appl. Math., 78 (2018), pp. 2865–2890, <https://doi.org/10.1137/18M1182218>.
- [2] S. AGARWAL, K. MIERLE, AND OTHERS, *Ceres solver*. <http://ceres-solver.org>.
- [3] R. J. ASTLEY, *Infinite elements for wave problems: a review of current formulations and an assessment of accuracy*, Internat. J. Numer. Methods Engrg., 49 (2000), pp. 951–976, [https://doi.org/10.1002/1097-0207\(20001110\)49:7\(951::AID-NME989\)3.0.CO;2-T](https://doi.org/10.1002/1097-0207(20001110)49:7(951::AID-NME989)3.0.CO;2-T).

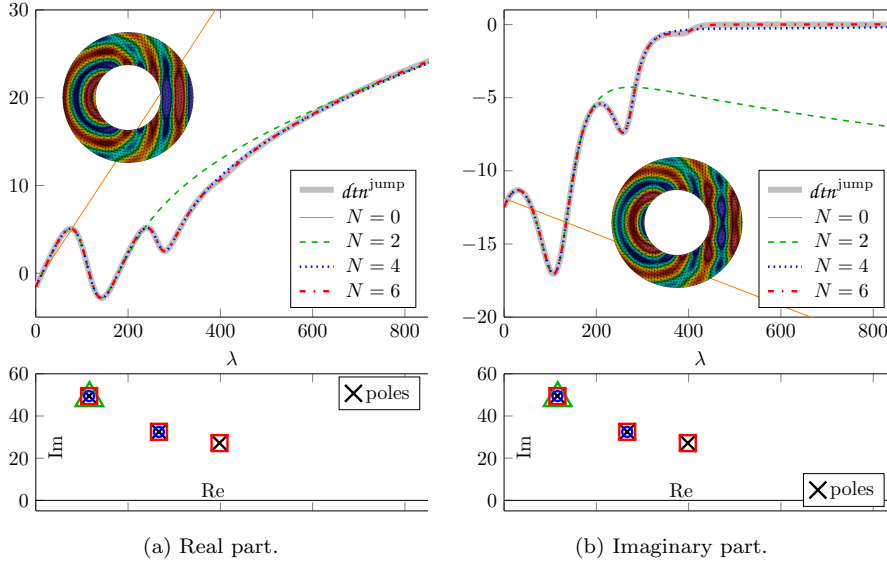


FIG. 12. Approximation results for the imaginary part of dtn belonging to a discontinuous exterior wavespeed which jumps from $k_I = 16$ to $k_\infty = 12$.

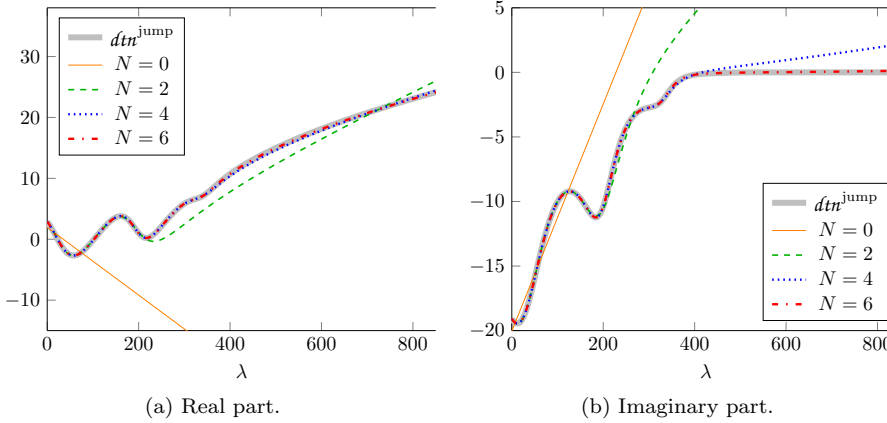


FIG. 13. Approximation results for the imaginary part of dtn belonging to a discontinuous exterior wavespeed which jumps from $k_I = 16$ to $k_\infty = 20$.

- [4] H. BARUCQ, J. CHABASSIER, M. DURUFLÉ, L. GIZON, AND M. LEGUÈBE, *Atmospheric radiation boundary conditions for the Helmholtz equation*, ESAIM: M2AN, 52 (2018), pp. 945–964, <https://doi.org/10.1051/m2an/2017059>.
- [5] H. BARUCQ, F. FAUCHER, AND H. PHAM, *Outgoing solutions and radiation boundary conditions for the ideal atmospheric scalar wave equation in helioseismology*, ESAIM Math. Model. Numer. Anal., (2020), pp. 1111–1138, <https://doi.org/10.1051/m2an/2019088>.
- [6] A. BAYLISS AND E. TURKEL, *Radiation boundary conditions for wave-like equations*, Comm. Pure Appl. Math., 33 (1980), pp. 707–725, <https://doi.org/10.1002/cpa.3160330603>.
- [7] J.-P. BERENGER, *A perfectly matched layer for the absorption of electromagnetic waves*, J. Comput. Phys., 114 (1994), pp. 185 – 200, <https://doi.org/https://doi.org/10.1006/jcph.1994.1159>.
- [8] P. BETTRESS, *Infinite elements*, Internat. J. Numer. Methods Engrg., 11 (1977), pp. 53–64,

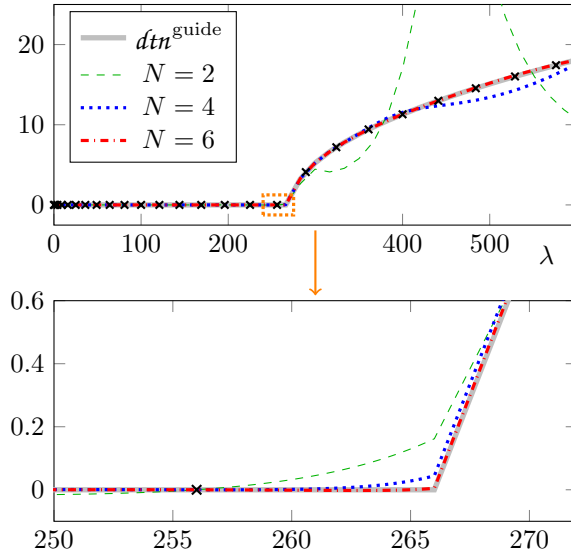


FIG. 14. Approximation results for real part of dt_n^{guide} with $k = 16.5$. The sample points $dt_n^{\text{guide}}(\lambda_\ell)$ are displayed as black crosses.

- <https://doi.org/10.1002/nme.1620110107>.
- [9] Z. CHEN AND X. LIU, *An Adaptive Perfectly Matched Layer Technique for Time-Harmonic Scattering Problems*, SIAM J. Numer. Anal., 43 (2006), pp. 645–671, <https://doi.org/10.1137/040610337>.
 - [10] J. CHRISTENSEN-DALSGAARD ET AL., *The current state of solar modeling*, Science, 272 (1996), pp. 1286–1292, <https://doi.org/10.1126/science.272.5266.1286>.
 - [11] F. COLLINO AND P. MONK, *The perfectly matched layer in curvilinear coordinates*, SIAM J. Sci. Comput., 19 (1998), p. 2061–2090, <https://doi.org/10.1137/S1064827596301406>.
 - [12] D. COLTON AND R. KRESS, *Inverse Acoustic and Electromagnetic Scattering Theory*, Springer, Berlin, Heidelberg, New York, forth ed., 2019, <https://doi.org/10.1007/978-3-030-30351-8>.
 - [13] V. DANCHENKO, M. KOMAROV, AND P. CHUNAIEV, *Extremal and approximative properties of simple partial fractions*, Russian Math.(Iz. VUZ), 62 (2018), pp. 6–41, <https://doi.org/10.3103/S1066369X18120022>.
 - [14] L. DEMKOWICZ AND K. GERDES, *Convergence of the infinite element methods for the Helmholtz equation in separable domains*, Numer. Math., 79 (1998), pp. 11–42, <https://doi.org/10.1007/s002110050330>.
 - [15] B. ENGQUIST AND A. MAJDA, *Radiation boundary conditions for acoustic and elastic wave calculations*, Comm. Pure Appl. Math., 32 (1979), pp. 314–358, <https://doi.org/10.1002/cpa.3160320303>.
 - [16] D. FOURNIER, M. LEGUÈBE, C. S. HANSON, L. GIZON, H. BARUCQ, J. CHABASSIER, AND M. DURUFLÉ, *Atmospheric-radiation boundary conditions for high-frequency waves in time-distance helioseismology*, A&A, 608 (2017), A109, p. A109, <https://doi.org/10.1051/0004-6361/201731283>.
 - [17] D. GIVOLI, *Recent advances in the DtN FE Method*, Arch. Comput. Methods Eng., 6 (1999), pp. 71–116, <https://doi.org/10.1007/BF02736182>.
 - [18] D. GIVOLI, *High-order local non-reflecting boundary conditions: a review*, Wave Motion, 39 (2004), pp. 319 – 326, <https://doi.org/https://doi.org/10.1016/j.wavemoti.2003.12.004>. New computational methods for wave propagation.
 - [19] D. GIVOLI AND I. PATLASHENKO, *Optimal local non-reflecting boundary conditions*, Appl. Numer. Math., 27 (1998), pp. 367–384, [https://doi.org/https://doi.org/10.1016/S0168-9274\(98\)00020-8](https://doi.org/https://doi.org/10.1016/S0168-9274(98)00020-8). Special Issue on Absorbing Boundary Conditions.
 - [20] D. GIVOLI AND I. PATLASHENKO, *An optimal high-order non-reflecting finite element scheme for wave scattering problems*, Int. J. Numer. Meth. Engng., 53 (2002), pp. 2389–2411, <https://doi.org/https://doi.org/10.1002/nme.406>.
 - [21] L. GIZON, H. BARUCQ, M. DURUFLÉ, C. S. HANSON, M. LEGUÈBE, A. C. BIRCH, J. CHABASSIER,

- D. FOURNIER, T. HOHAGE, AND E. PAPINI, *Computational helioseismology in the frequency domain: acoustic waves in axisymmetric solar models with flows*, A&A, 600 (2017), p. A35, <https://doi.org/10.1051/0004-6361/201629470>.
- [22] L. GIZON AND A. C. BIRCH, *Local Helioseismology*, Living Rev. Sol. Phys., 2 (2005), 6, <https://doi.org/10.12942/lrsp-2005-6>.
- [23] L. GIZON, A. C. BIRCH, AND H. C. SPRUIT, *Local helioseismology: Three-dimensional imaging of the solar interior*, ARA&A, 48 (2010), pp. 289–338, <https://doi.org/10.1146/annurev-astro-082708-101722>.
- [24] N. A. GUMEROV AND R. DURAISWAMI, *Fast multipole methods for the Helmholtz equation in three dimensions*, Elsevier, 2005, <https://doi.org/10.1016/B978-0-08-044371-3.X5000-5>.
- [25] T. HAGSTROM, *Radiation boundary conditions for the numerical simulation of waves*, Acta Numer., 8 (1999), pp. 47–106, <https://doi.org/10.1017/S0962492900002890>.
- [26] T. HOHAGE, C. LEHRENFELD, AND J. PREUSS, *Learned infinite elements: Live notebooks*, May 2021, https://mybinder.org/v2/git/https%3A%2F%2Fgitlab.gwdg.de%2Flearned_infinite_elements%2Flearned_ie/master?filepath=notebooks%2Foverview.ipynb.
- [27] T. HOHAGE, C. LEHRENFELD, AND J. PREUSS, *Replication data for: Learned infinite elements*, May 2021, <https://doi.org/10.25625/XPLPRR>.
- [28] T. HOHAGE AND L. NANNEN, *Hardy Space Infinite Elements for Scattering and Resonance Problems*, SIAM J. Numer. Anal., 47 (2009), pp. 972–996, <https://doi.org/10.1137/070708044>.
- [29] F. IHLENBURG, *Finite Element Analysis of Acoustic Scattering*, Appl. Math. Sci. 132, Springer, New York, 1998, <https://doi.org/10.1007/b98828>.
- [30] F. JOHANSSON ET AL., *mpmath: a Python library for arbitrary-precision floating-point arithmetic*, December 2013. <http://mpmath.org/>.
- [31] O. N. KOSUKHIN, *Approximation properties of the most simple fractions.*, Vestnik Moskov. Univ. Ser. 1. Mat. Mekh., (2001), pp. 54–59.
- [32] P. KOWALCZYK, *Complex Root Finding Algorithm Based on Delaunay Triangulation*, ACM Trans. Math. Softw., 41 (2015), <https://doi.org/10.1145/2699457>.
- [33] P. KOWALCZYK, *Global Complex Roots and Poles Finding Algorithm Based on Phase Analysis for Propagation and Radiation Problems*, IEEE Trans. Antennas and Propagation, 66 (2018), pp. 7198–7205, <https://doi.org/10.1109/TAP.2018.2869213>.
- [34] W. MAGNUS AND L. KOTIN, *The Zeros of the Hankel Function as a Function of Its Order*, Numer. Math., 2 (1960), p. 228–244, <https://doi.org/10.1007/BF01386226>.
- [35] D. J. NEWMAN, *Rational approximation to $|x|$* , Michigan Math. J., 11 (1964), pp. 11–14, <https://doi.org/10.1307/mmj/1028999029>.
- [36] J. SCHÖBERL, *NETGEN An advancing front 2D/3D-mesh generator based on abstract rules*, Comput. Vis. Sci., 1 (1997), pp. 41–52, <https://doi.org/10.1007/s007910050004>.
- [37] J. SCHÖBERL, *C++11 implementation of finite elements in NGSolve*, tech. report, ASC-2014-30, Institute for Analysis and Scientific Computing; Karlsplatz 13, 1040 Vienna, Austria, September 2014.
- [38] A. TOSELLI AND O. WIDLUND, *Domain Decomposition Methods – Algorithms and Theory*, vol. 34, Springer Series in Computational Mathematics, 2005, <https://doi.org/10.1007/b137868>.
- [39] R. F. UNGLESS, *Infinite finite element*, master’s thesis, University of British Columbia, 1973, <https://doi.org/http://dx.doi.org/10.14288/1.0050530>.
- [40] J. E. VERNAZZA, E. H. AVRETT, AND R. LOESER, *Structure of the solar chromosphere. III. Models of the EUV brightness components of the quiet sun.*, ApJ, 45 (1981), pp. 635–725, <https://doi.org/10.1086/190731>.
- [41] J. L. WALSH, *Interpolation and approximation by rational functions in the complex domain; 3rd ed.*, Colloquium publications, American Mathematical Society, Providence, RI, 1960.